Catalysis Science & Technology

ROYAL SOCIETY OF CHEMISTRY

PAPER

View Article Online
View Journal | View Issue

Cite this: *Catal. Sci. Technol.*, 2024, 14, 6393

Multiscale modelling of CO_2 hydrogenation of TiO_2-supported Ni_8 clusters: on the influence of anatase and rutile polymorphs†

Lulu Chen, Ying-Ying Ye, Rozemarijn D. E. Krösschell, Emiel J. M. Hensen and Ivo A. W. Filot *

Received 6th May 2024,
Accepted 15th September 2024

DOI: 10.1039/d4cy00586d

rsc.li/catalysis

The selection of TiO_2 phase, whether anatase or rutile, for supporting small Ni clusters significantly influences the activity and selectivity in CO_2 hydrogenation to methane. To model and understand these variances, we developed a hierarchical multiscale catalytic model. Utilizing a hybrid approach combining genetic algorithms and density functional theory, we identified the putative global minimum structures of Ni_8 clusters supported on anatase (Ni_8/TiO_2-a) and rutile (Ni_8/TiO_2-r), which are morphologically distinct. Microkinetics simulations based on the energetics derived from DFT calculations over these distinct clusters reveal the mechanism of CO_2 hydrogenation to CO, CH_4 and CH_3OH. On both Ni_8/TiO_2-a and Ni_8/TiO_2-r, CH_4 is the main product at low temperature while a shift to CO occurs with increasing temperature. In comparison to Ni_8/TiO_2-r, Ni_8/TiO_2-a exhibits a higher activity and keeps a higher selectivity towards CH_4 with increasing temperature. Using a sensitivity analysis, we identify the steps responsible for the observed selectivity difference and rationalize the observed barrier differences for these steps between the different clusters by means of detailed electronic structure analysis.

1. Introduction

In recent decades, the escalating levels of atmospheric carbon dioxide (CO_2) contribute significantly to rising global temperatures, sea-level rise, altered weather patterns, and various ecological disruptions. To mitigate these adverse effects and transition towards a more sustainable and carbon-neutral future, innovative approaches and technologies capable of reducing CO_2 emissions at scale are required.[1–5] Sustainably produced hydrogen, for example from excess wind and solar power, can be utilized to convert CO_2 to CH_4 in the so-called power-to-gas concept.[6–8] An important benefit of CH_4 is that existing infrastructure for storage and transport can be repurposed.[6,9]

For the practical implementation of CO_2 hydrogenation to CH_4, catalysts are essential to ensure both high reaction rates and selectivity towards the desired product. While methanation catalysts have been extensively studied, Ru stands out for its superior performance among investigated transition metals.[10,11] However, the widespread industrial application of Ru catalysts is hindered by its relatively high cost. In contrast, Co and Ni also demonstrate high conversion rates in CO_2 methanation, with Ni being the preferred choice for industrial applications, as it is the cheaper of the two metals.[12–14]

The activity of supported transition metal catalysts is affected by many factors, with the size of the nanoparticles being a dominant one, strongly affecting the abundance of specific surface atom arrangements relevant to dissociation and association reactions below 10 nm.[15] The effect of nanoparticle size on the activity and selectivity of CO_2 hydrogenation to CO and CH_4 remains a topic of intense debate. Two dominant trends can be identified in the literature. Some studies show an increased surface-normalized CO_2 conversion with increasing particle size,[16–21] while others find an optimum.[22–24] In a recent study of Simons *et al.*, it was found that Ni-catalyzed CO_2 methanation uses two different types of active sites, one for reverse-water-gas-shift (RWGS) reaction yielding intermediary CO and another type of site for CO conversion to methane. While RWGS is structure-independent, the activity of CO methanation shows strong structure-dependence caused by the particle size dictating the abundancy of this latter type of active site.[25]

In addition to nanoparticle size, the support material can influence the morphology of the nanoparticles. Apart from the wetting properties of the support affecting the nanoparticle, the surface structure of the support also has an epitaxial effect that influences nanoparticle morphology by favoring specific

Laboratory of Inorganic Materials and Catalysis, Department of Chemical Engineering and Chemistry, Eindhoven University of Technology, P.O. Box 513, 5600 MB Eindhoven, The Netherlands. E-mail: i.a.w.filot@tue.nl

† Electronic supplementary information (ESI) available. See DOI: https://doi.org/10.1039/d4cy00586d

alignments at the support–nanoparticle interface.[26–29] A notable example is found when using TiO_2 as a support material, which exists in three primary crystalline forms, being anatase, rutile and brookite. CO_2 methanation catalyzed by TiO_2-supported nanoparticles show different activity and selectivity trends based on the phase of TiO_2.[30–33] Li *et al.* showed that for similarly sized Co nanoparticles (~20 nm), the anatase-supported particles mainly produce CO under CO_2 hydrogenation conditions, while the rutile-supported counterpart exhibits high methane selectivity.[30] Wang *et al.* reported a similar effect for small Ru nanoparticles (~2–3 nm), where the rutile phase is significantly more active and selective towards CH_4 than the anatase phase. This enhanced selectivity is assigned to the formation of a favorable overlayer structure guided by the interfacial compatibility between the RuO_2 precursor phase and rutile, prior to reduction. In contrast, on anatase only small nanoparticles are formed.[32] Likewise, the works of Lin *et al.* and Messou *et al.* observe for similarly sized Ni nanoparticles (~30 nm) an increased activity and selectivity towards CH_4 for the rutile phase over the anatase phase in CO_2 hydrogenation. The increased activity is assigned to the rutile phase giving rise to Ni nanoparticles that portray facile CO dissociation and H_2 activation.[31,33]

Clearly, the choice of TiO_2 phase, whether anatase or rutile, has a strong impact on the catalytic activity, even when the nanoparticles are roughly the same size. Different support materials, their phases and surface termination determine the metal–support interaction strength and thus modulate particle sizes invoking known structure sensitivity patterns. When nanoparticle sizes remain comparable between different support structures, yet a different kinetic response is observed, this is a strong indicator that the support influences the particle shape. Computational catalysis can aid in understanding these effects, yet the scale of these systems remains still prohibitively large for detailed electronic structure calculations. One way to tackle this is by means of DFT-based force fields, as performed earlier by us for both unsupported Co nanoparticles[26] as well as Co nanoparticles on a model support material.[34] In this work, rather than producing such a force field, the system is made computationally accessible by focusing on small Ni clusters. Small Ni clusters provide an excellent model system to study active site configurations that are guided by the alignment of the support substructure.

To understand and characterize how support effects can influence the activity and selectivity in CO_2 hydrogenation to methane for small clusters, we construct a multiscale model for Ni_8 clusters supported on rutile and anatase. Although experimentally always a range of particle size distributions is observed, these small Ni_8 clusters are representative for particle sizes below 1 nm. By means of a DFT-based genetic algorithm in conjunction with machine learning, we explore the configuration space of TiO_2-supported Ni_8 clusters and identify the putative global minimum configuration. Next, the kinetic pathways for CO_2 hydrogenation to CH_4 are calculated. By means of microkinetics simulations, we found that Ni_8/TiO_2-anatase in comparison to Ni_8/TiO_2-rutile exhibits a much higher activity while also portraying a higher selectivity to CH_4 with increasing temperature. Using a sensitivity analysis, we identified that the preferred manner of C–O bond scission – hydrogen-assisted pathway *via* HCO* for Ni_8/TiO_2-anatase, while in a direct fashion for Ni_8/TiO_2-rutile – dictates the observed activity and selectivity differences. These differences are caused by the specific topology of the active site dictated by the alignment of Ni atoms with the support structure. By means of a crystal orbital Hamilton population analysis, the difference in barrier for CO dissociation is rationalized. This study adds to our understanding by which mechanism the catalyst support can modulate the catalytic reaction.

2. Methods

2.1 DFT calculations

All density functional theory (DFT) calculations were performed using the Perdew–Burke–Ernzerhof (PBE) exchange–correlation functional[35] as implemented in the Vienna *ab initio* simulation package (VASP) software.[36,37] All DFT calculations were conducted with spin-polarization taken into account. The interaction of the core-electrons and nucleus was described with the Projector Augmented Wave (PAW) method.[38–40] The cut-off energy was set to 400 eV. The Brillouin zone was sampled using a 1 × 1 × 1 grid. Gaussian smearing with a width of 0.05 eV determined partial occupancies for each orbital. Ionic convergence was achieved when the forces were smaller than 0.05 eV $Å^{-1}$ for each atom in each Cartesian direction. A Van-der-Waals correction was added to our calculation using the DFT-D3 method with the Becke–Johnson damping function.[41,42] Climbing image nudged elastic band (CI-NEB) was employed to investigate the transition pathway.[43,44] The transition state was optimized using a quasi-Newton algorithm and the optimized geometry was examined by vibrational mode analysis. It was verified that all transition states have a single imaginary mode in the direction of the reaction coordinate. We employed a finite difference approach to construct the Hessian matrix for frequency analysis by perturbing the atomic positions by 0.01 Å in each Cartesian direction. Furthermore, the vibrational mode analysis was used to construct zero-point energy corrections.

2.2 Structural models

For anatase and rutile TiO_2, the periodically repeated (101) and (110) surface terminations were employed as supports for Ni_8 clusters, as these surfaces are known to be the most thermodynamically stable for their respective phases.[45,46] Ni_8 clusters deposited on (101) surface of TiO_2 anatase and (110) surface of TiO_2 rutile are denoted as Ni_8/TiO_2-a and Ni_8/TiO_2-r, respectively. We specifically selected Ni_8 clusters because they are large enough to potentially support step-edge configurations, which are known to promote C–O bond scission.[47] However, this does not guarantee that these active site patterns are thermodynamically favorable, as the support interface also plays a crucial role. Nevertheless, choosing smaller cluster sizes would *a priori* prevent studying such sites.

The lattice parameters of TiO_2-a and TiO_2-r bulks were optimized and found to be 3.816 Å × 3.816 Å × 9.539 Å and 4.650 Å × 4.650 Å × 2.966 Å, respectively. These optimized lattice parameters are in good agreement with the values obtained from experimental results.[48,49] For TiO_2-a, a 1 × 3 (101) surface termination with dimensions of 10.42 Å × 11.46 Å was constructed. Its slab model hosts three O–Ti–O layers with the bottom layer fixed while the top two layers are allowed to relax.[50] For Ni_8/TiO_2-r, a 5 × 2 (110) surface termination with dimensions of 14.85 Å × 13.18 Å was constructed. The corresponding slab model has four O–Ti–O layers. The bottom layer was fixed while the top three layers were allowed to perturb. To avoid the spurious interaction of neighboring supercells in the *z*-direction, the TiO_2-a and TiO_2-r super cells have a vacuum space of at least 15 Å. A depiction of the supercells is given in the ESI† in Fig. S1.

2.3 Genetic algorithm

In order to search for the putative global minimum structure of Ni_8 clusters deposited on the anatase (101) and rutile (110) surface of TiO_2, a GA-DFT algorithm based on the approach as described by Hammer *et al.* was employed.[51] In this approach, an ensemble of cluster configurations is procedurally generated and the stability of these clusters on the surface is assessed by DFT calculations. To efficiently probe the configuration space of cluster configurations, a genetic algorithm method is used wherein new cluster configurations are generated by a sequence of operations including translations, rotations, atomic migrations and mixing of clusters. For each generation, at least 12 candidates are generated to form the next generation. To enhance the diversity of the population, approximately 30% to 50% of the structures are mutated. Each cluster is subjected to a geometry optimization in a conventional DFT simulation and based on the energies of the clusters they are ranked in terms of stability. New generations of clusters are derived from an older generation using stability and similarity metrics. This yields a strong (*i.e.* containing many stable structures) yet sufficiently diverse population between all iterations. The algorithm is considered to be converged when no new more stable configurations are found for a number of generations, typically between 5–10. Details of the GA-DFT procedure can be found in the earlier work of Chang *et al.*[52]

To assess the similarity of the clusters and identify common shapes, an unsupervised non-linear dimensionality reduction was conducted *via* the *t*-distributed stochastic neighbor embedding (*t*-SNE) method as implemented in the sklearn Python library.[53,54] The dimensionality reduction is applied to a $N \times N$ square distance metric matrix M with N being the number of clusters. Each element in M corresponds to the minimized Hilbert–Schmidt norm[55] of the distance-difference matrix between two clusters. The minimized Hilbert–Schmidt norm is constructed by first constructing an atomic distance matrix $\boldsymbol{R}$ for each cluster.

$$\boldsymbol{R} = \begin{pmatrix} 0 & \cdots & r_{ij} \\ \vdots & \ddots & \vdots \\ r_{ji} & \cdots & 0 \end{pmatrix}, \tag{1}$$

wherein r_{ij} is the Euclidean distance between atom i and atom j in a cluster. As such, the matrix $\boldsymbol{R}$ is symmetric and has zeros on its diagonal. Given two atomic distance matrices $\boldsymbol{R}_k$ and $\boldsymbol{R}_l$ for clusters k and l, a similarity metric S_{kl} can be constructed by evaluating

$$S_{kl} = \sqrt{\sum_{ij} \left(r_{ij}^{(k)} - r_{ij}^{(l)}\right)^2}. \tag{2}$$

Although the distance matrix $\boldsymbol{R}$ is translationally and rotationally invariant, it is not permutationally invariant and as such, the value of S_{kl} depends on the specific indexing of the atoms. Consequently, the value of S_{kl} needs to be minimized by considering all possible permutations of the atomic indices for one of the clusters. Given the small number of atoms in the clusters, it is possible to employ a brute force approach wherein all 8! = 40 320 permutations were explicitly considered. The lowest value found, *i.e.* $S_{kl,\min}$, is then used as the elements to construct M. For the construction of M, we used the in-house developed program Bramble which employs a GPU-accelerated procedure to evaluate all permutations.[56]

2.4 Microkinetics simulations

Microkinetics simulations based on DFT-derived reaction networks were conducted to determine the catalytic performance of Ni_8/TiO_2-a and Ni_8/TiO_2-r for CO_2 hydrogenation. All microkinetics simulations were performed using the in-house developed MKMCXX program.[57,58] For each elementary reaction step in the chemokinetic network as given by

$$\nu_a A + \nu_b B \underset{k^-}{\overset{k^+}{\rightleftharpoons}} \nu_c C + \nu_d D, \tag{3}$$

a corresponding rate expression, *i.e.* an ordinary differential equation in time, can be constructed by

$$r_A = -\frac{d[A]}{dt} = \nu_a \left(k^+ [A]^{\nu_a} [B]^{\nu_b} - k^- [C]^{\nu_c} [D]^{\nu_d}\right) \tag{4}$$

Herein, ν_X is the stoichiometric coefficient of component X and k^+ and k^- are the rate constants for the forward and backward reaction, respectively. From harmonic transition state theory, the reaction rate constants are calculated by the Eyring equation

$$k = \frac{k_B T}{h} \frac{f_{TS}^{\#}}{f_{IS}} \exp\left(-\frac{\Delta E_a}{k_B T}\right) \tag{5}$$

wherein h is the Planck constant, ΔE_a the activation energy, k_B the Boltzmann constant, T the temperature, and finally $f_{TS}^{\#}$ and f_{IS} are the partition functions of the transition state and the initial state, respectively.

For the adsorption steps, it is assumed that the adsorbing molecule loses one of the translational degrees of freedom with respect to the initial state. The rate constant for

adsorption is then determined by the rate of surface impingement of gas-phase molecules for non-activated molecular adsorption and is given by[59]

$$k_{ads} = \frac{PA}{\sqrt{2\pi m k_B T}}, \quad (6)$$

wherein P corresponds to the partial pressure of the adsorbate in the gas phase, A the effective surface area of the adsorption site, and m the mass of the adsorbate.

Considering the reversibility of the adsorption step, the molecule regains all its rotational degrees of freedom (*i.e.* three degrees of freedom for non-linear molecules and two degrees of freedom for linear molecules) and two translational degrees of freedom in the desorption step. Therefore, the desorption rate is given by

$$k_{des} = \frac{k_B T}{h} \frac{q_{vib,gas} q_{rot,gas} q_{tran2D,gas}}{q_{vib,ads}} \exp\left(\frac{\Delta E_{ads}}{k_B T}\right) \quad (7)$$

wherein ΔE_{ads} is the adsorption energy. $q_{vib,gas}$, $q_{rot,gas}$ and $q_{tran2D,gas}$ represent the vibrational, rotational and two-dimensional translation partition function of a molecule in gas phases, respectively. $q_{vib,ads}$ refers to the vibrational partition function of the molecule upon adsorption.

In our simulations, the initial gas phase contained a mixture of CO_2 and H_2 in a 1 : 4 ratio at a total pressure of 1 atm, in line with the conditions used in the experiment.[60] To identify the elementary reaction steps that control the overall rate of CO_2 consumption, Campbell's degree of rate control analysis was employed.[61]

3. Results and discussions

3.1 Ni_8 clusters supported on anatase and rutile TiO_2

To find the most stable structures for Ni_8 clusters supported on anatase and rutile TiO_2, a GA-DFT algorithm was employed which produced 244 and 104 candidate structures for the anatase and rutile systems, respectively. The candidates were ranked based on the total energy of the system. The 10 most stable structures for anatase and rutile TiO_2 are given in Fig. S2 and S4,† respectively. To investigate whether there are multiple cluster configurations that are topologically distinct yet portray a similar stability on the surface, a similarity analysis was conducted by calculating the minimized Hilbert–Schmidt norm between all clusters. Using a non-linear dimensionality reduction based on the *t*-SNE method, we could classify all clusters into distinct categories as shown in Fig. 1. Representative cluster configurations for each of these groups are shown in Fig. 1 as well.

The most stable Ni cluster on the anatase TiO_2 (101) surface, representative of group 1, adopts a bilayer configuration in which 6 Ni atoms are located in the bottom layer forming two fourfold type of adsorption sites on which the two atoms of the top layer are located. The clusters in groups 2–4 exhibit fewer Ni atoms binding to the O atoms of the support and are higher in energy. In Fig. S3,† the 9 most similar clusters with respect to the most stable cluster are shown. We can readily observe that these structures are related to the most stable structure either *via* a rotation or *via* a migration of one or two Ni atoms.

On the rutile TiO_2 (110) surface, the most stable cluster of Ni_8 also adopts a bilayer configuration. In contrast to the anatase system, the bottom layer has a triangular shape exposing four threefold adsorption sites. The top layer is constructed by the adsorption of two Ni atoms on two of these threefold adsorption sites. The *t*-SNE manifold learning shows that, for this system, also four distinct groups of clusters are found. The most stable configuration belongs to group 1, group 2 shows a different configuration yet similar to group 1 on anatase TiO_2(101) with 6 atoms in the bottom layer and two atoms in the top layer. In contrast, groups 3 and 4 show a configuration with 5 atoms in the bottom layer and 3 in the top layer. Groups 2, 3 and 4 are, on average, higher in energy than group 1 as they either lack a strong interaction with the support (groups 3 and 4) or have more undercoordinated metal atoms (group 2).

Furthermore, due to known SMSI effects, we also investigated planar Ni_8 clusters that optimize the contact area between the TiO_2-support and the Ni_8 cluster. The configurations are shown in Fig. S6 in the ESI.† It was found that on both TiO_2 anatase and rutile, a planar Ni_8 cluster is less stable than a non-planar cluster by 1.35 eV and 1.06 eV, respectively. As such, we proceeded with evaluating the elementary reaction steps for CO_2 hydrogenation using non-planar cluster configurations.

3.2 Chemical reactivity of CO_2 hydrogenation over Ni_8/TiO_2-a and Ni_8/TiO_2-r

3.2.1 Adsorption of CO_2 and H_2. In Fig. 2, the two most stable cluster configurations for anatase and rutile are shown. To label the different types of active sites involved in the mechanism, we employ the following notations:

- T_i: the top site of Ni_i.
- B_{i-j}: the bridge site located between N_i and Ni_j.
- H_{i-j-k}: the hollow site that comprises Ni_i, Ni_j, and Ni_k.
- $F_{i-j-k-l}$: the four-fold site formed by Ni_i, Ni_j, Ni_k, and Ni_l.

First, the preferred adsorption configurations of CO_2 and H_2 on the various active sites are explored. For H_2, we considered both molecular as well as dissociative adsorption. In Fig. 3 and 4, an overview is given of the different adsorption modes and corresponding adsorption energies of CO_2 and H_2 on Ni_8/TiO_2-a and Ni_8/TiO_2-r, respectively. From the results in Fig. 3 and 4, it can be seen that dissociative H_2 adsorption is more exothermic as compared to molecular adsorption and the H atoms preferentially reside at the metal–support interface. The most stable configurations for H_2 adsorption correspond to adsorption energies of ΔE_{ads} = −1.23 eV and ΔE_{ads} = −1.37 eV for Ni_8/TiO_2-a and Ni_8/TiO_2-r, respectively. In these configurations, H_2 is dissociatively adsorbed to form 2H*. This process is activated by 0.11 eV and 0.39 eV for Ni_8/TiO_2-a and Ni_8/TiO_2-r, respectively. These results are similar to H_2 dissociation on a Ni_{13} cluster (ΔE_{act} = 0.21 eV) and Ni/In_2O_3 (ΔE_{act} = 0.22 eV).[62,63] H spillover is

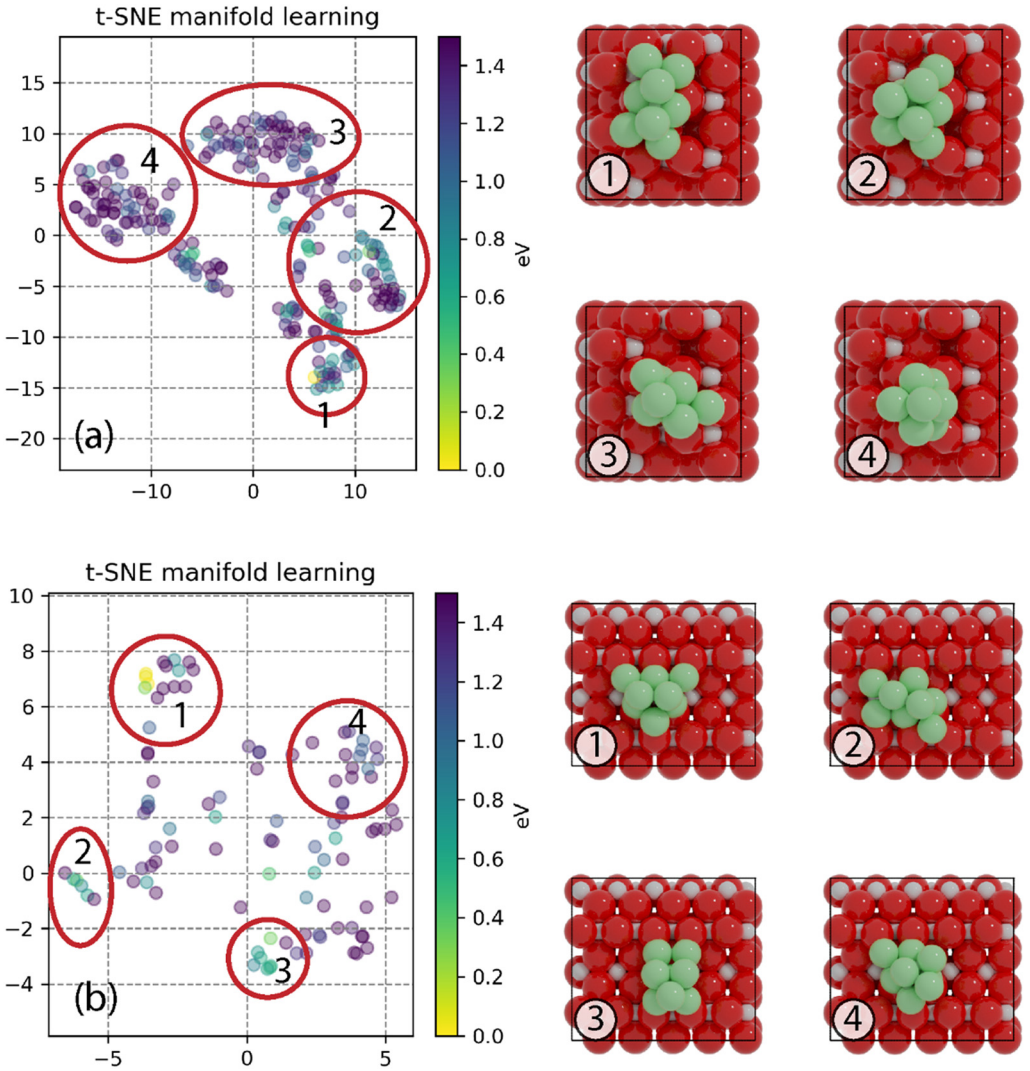

Fig. 1 *t*-SNE manifold learning of GA-DFT generated structures of Ni_8/TiO_2-a (a) and Ni_8/TiO_2-r (b), with clusters of similar structures encircled and labeled 1–4. Representative structures for each part are displayed on the right of *t*-SNE figures. Color codes: red: O; light gray: Ti; green: Ni. The energies of all structures relative to the most stable one are shown using a color map. The structure's stability decreases as the color transitions from yellow to purple.

commonly discussed experimentally.[64] Therefore, H spillover is also considered on these two models. As shown in Fig. S7,† H spillover occurs with activation energies of ΔE_{act} = 0.89 eV and ΔE_{act} = 1.09 eV on Ni_8/TiO_2-a and Ni_8/TiO_2-r, respectively.

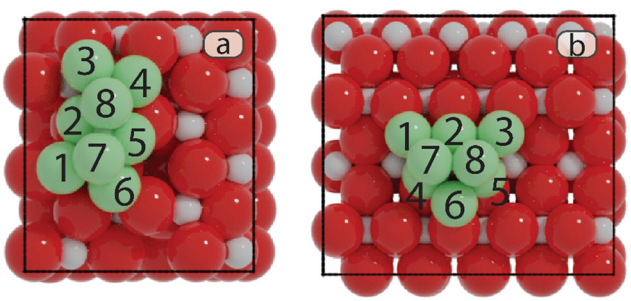

Fig. 2 The most stable models of Ni_8/TiO_2-a (a) and Ni_8/TiO_2-r (b). Color codes: red: O; light gray: Ti; green: Ni. The numbering of Ni atoms corresponds to the active sites as described in the main text.

This step is endothermic with reaction energies of ΔE_R = 0.67 eV and ΔE_R = 0.50 eV for Ni_8/TiO_2-a and Ni_8/TiO_2-r, respectively. Given the endothermic nature of the H spillover reaction and the fact that CO_2 adsorption takes place on Ni clusters (*vide infra*), H spillover is not further considered in the evaluation of the reaction mechanism. On Ni_8/TiO_2-a, CO_2 adsorption is preferred at the B_{7-8} or H_{5-7-8} sites, both sites yielding an adsorption energy of ΔE_{ads} = −0.93 eV. On Ni_8/TiO_2-r, the most stable site for CO_2 adsorption is H_{1-4-7} with an adsorption energy of ΔE_{ads} = −0.70 eV. Based on the preferred adsorption sites of H_2 and CO_2, we also considered the co-adsorption of CO_2 and H_2. For Ni_8/TiO_2-a we find a total adsorption energy of ΔE_{ads} = −2.39 eV, which is more exothermic than the sum of the individual CO_2 and H_2 adsorption energies. In a similar fashion, we find for Ni_8/TiO_2-r that the co-adsorbed state is more exothermic (ΔE_{ads} = −2.64 eV) than the sum of the individual adsorption energies. As these co-adsorbed states represent favorable adsorption

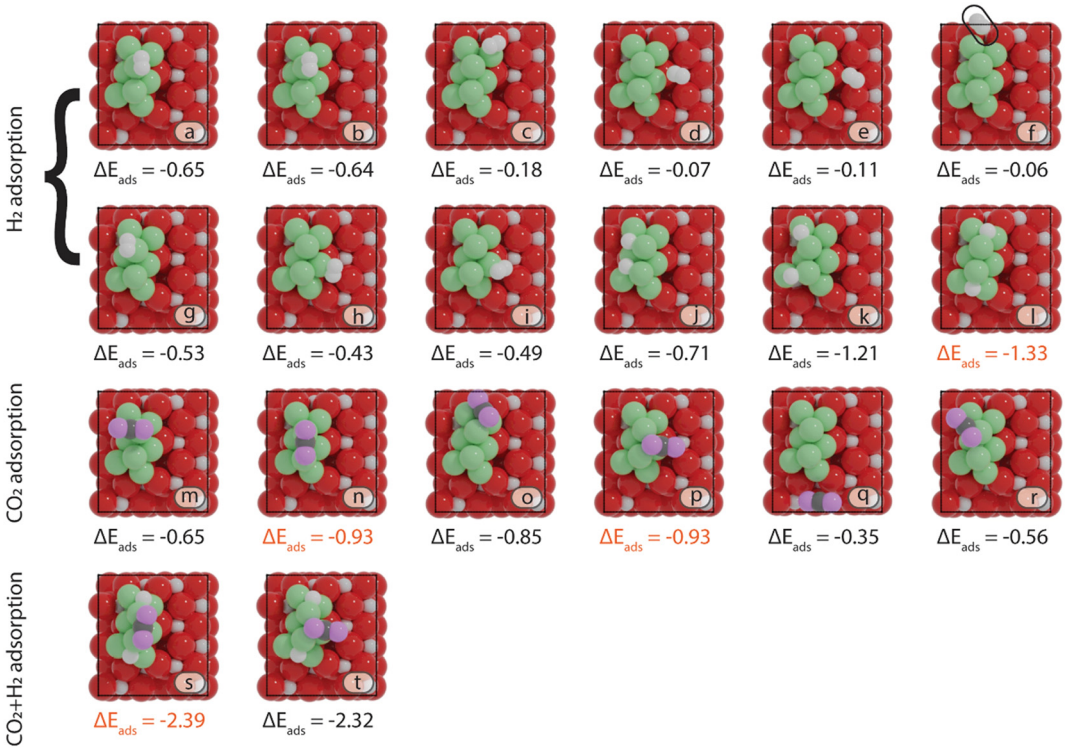

Fig. 3 Configurations of adsorbed H_2 (a–l), CO_2 (m–r) and co-adsorption of CO_2 and H_2 (s and t) on Ni_8/TiO_2-a. Color scheme: white: H; pink: O in CO_2; gray: C. A black border has been used to indicate the location of H_2 in f. The most stable configuration is indicated by the orange labels.

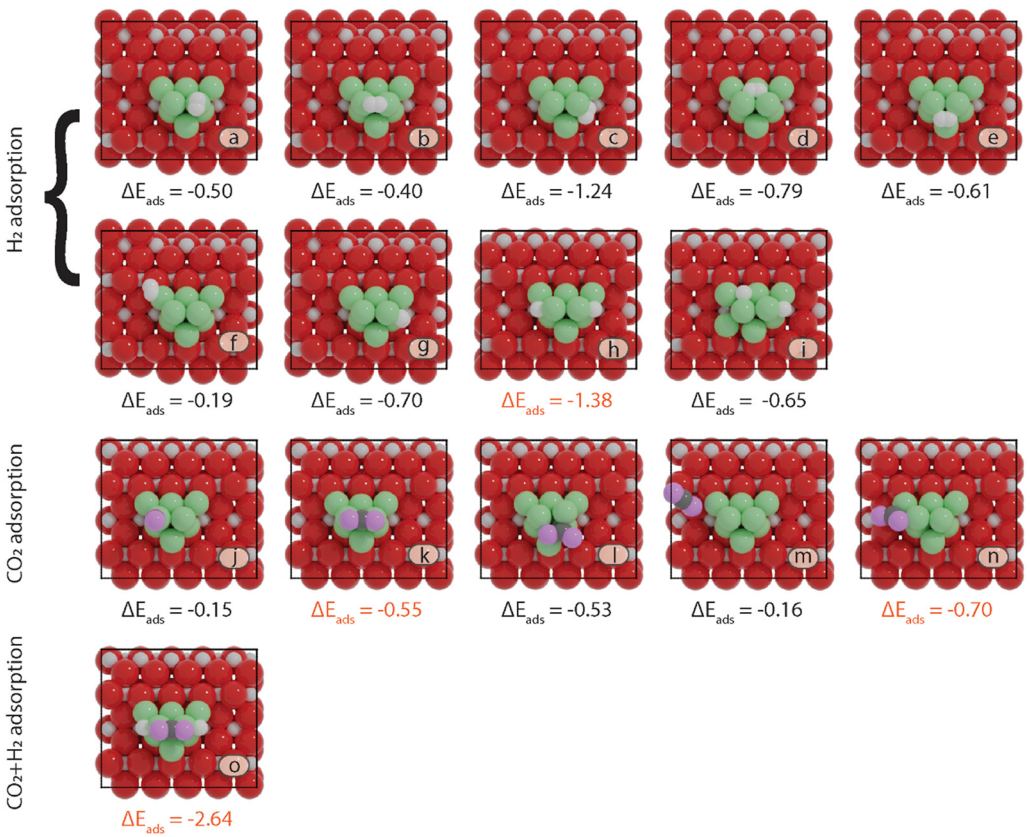

Fig. 4 Configurations of adsorbed H_2 (a–i), CO_2 (j–n) and co-adsorption of CO_2 and H_2 (o) on Ni_8/TiO_2-r. Color scheme: white: H; pink: O in CO_2; gray: C. The most stable configuration is indicated by the orange labels.

modes, we considered these in the further exploration of the reaction pathways.

3.2.2 CO_2 hydrogenation. We computed the reaction energetics of CO_2 hydrogenation to CH_4, CO, and CH_3OH on the most stable models identified in the previous section. The networks of elementary reaction steps and their forward and backward activation energies are displayed in Fig. 5 and 6 for Ni_8/TiO_2-a and Ni_8/TiO_2-r, respectively. In this section, we will explore the pathways related to elementary reaction steps involving CH_x and H_xCO intermediates in detail. Microkinetic simulations (as discussed later) revealed that the kinetic network associated with H_xCO_2 intermediates has a minimal impact on the overall reaction mechanism; therefore, this aspect is addressed in Sections S1 and S2 of the ESI.†

3.2.2.1 Ni_8/TiO_2-a

Pathway involving CH_x intermediates. We first discuss the elementary reaction steps among the CH_x intermediates (R1 to R19; brown section in Fig. 5) with CH_4 and CO as the main products. Initially, the reaction proceeds by adsorption and activation of H_2 (R1) and CO_2 (R2). Direct dissociation of CO_2^* (R3) needs to overcome an activation energy of 0.99 eV and this step is exothermic by 0.81 eV. After CO_2^* dissociation, the resulting O* is removed from the surface as H_2O *via* two consecutive hydrogenation steps. The H* located at H_{1-6-7} site reacts with O*, leading to the formation of OH* (R4, ΔE_{act} = 1.40 eV, ΔE_R = 0.26 eV). After a hydrogen migration step with a minor energy change (ΔE_R = 0.06 eV), the OH intermediate can be hydrogenated to H_2O (R5). Including the migration step, this step has activation and reaction energies of 1.39 eV and 1.07 eV, respectively. Finally, the desorption of H_2O (R6) is endothermic by ΔE_{des} = 0.94 eV, leaving an adsorbed CO* on Ni_8/TiO_2-a. This CO* species can either desorb from the surface (R7) with an energy of 1.93 eV or dissociate to form C* and O* (for H-assisted CO* dissociation, see below). It should be

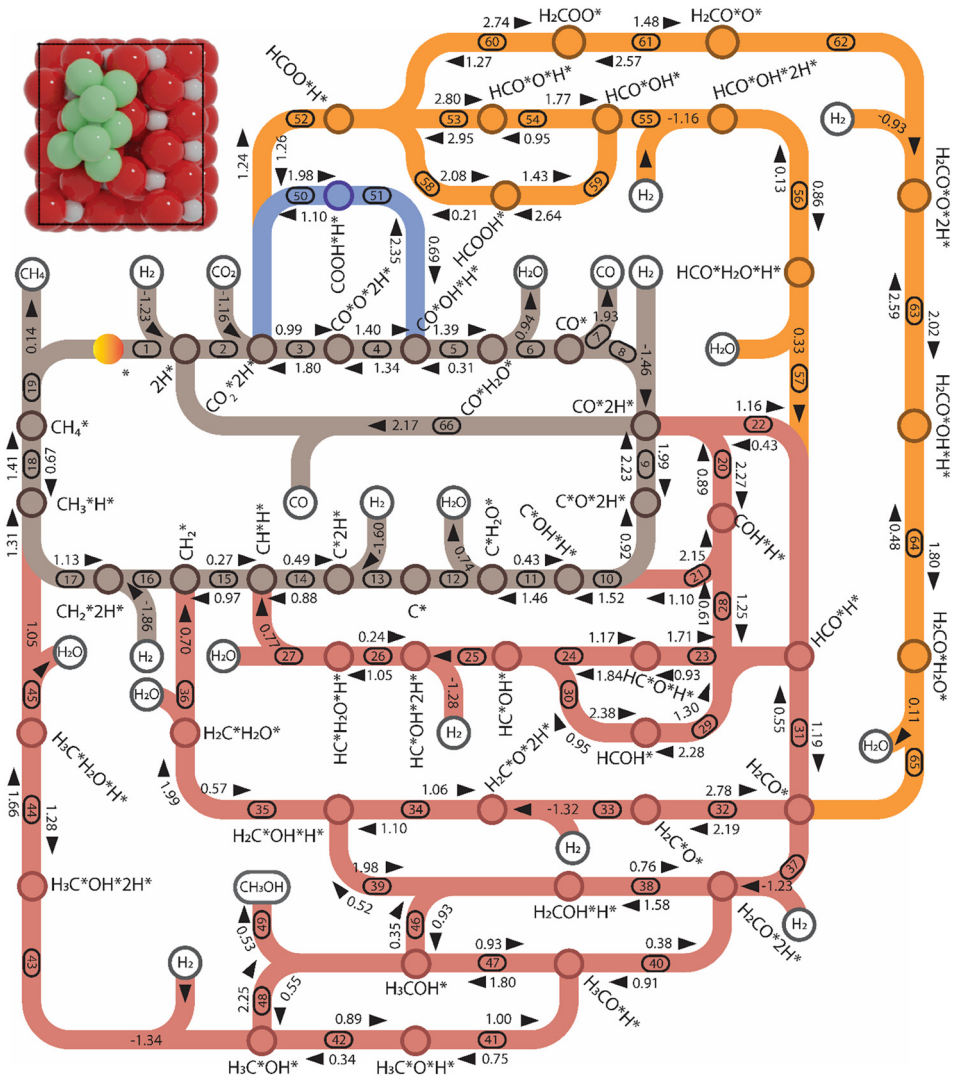

Fig. 5 Reaction network for CO_2 hydrogenation on Ni_8/TiO_2-a. The numbers correspond to the elementary reaction steps in Tables S1 and S2 and Fig. S8–S11.† The activation energy, adsorption energy, and desorption energy are reported in eV and include a zero-point energy correction (colors: brown: CH_x-intermediates pathway; red: H_xCO-intermediates pathway; and orange and blue: H_xCOO-intermediates pathways).

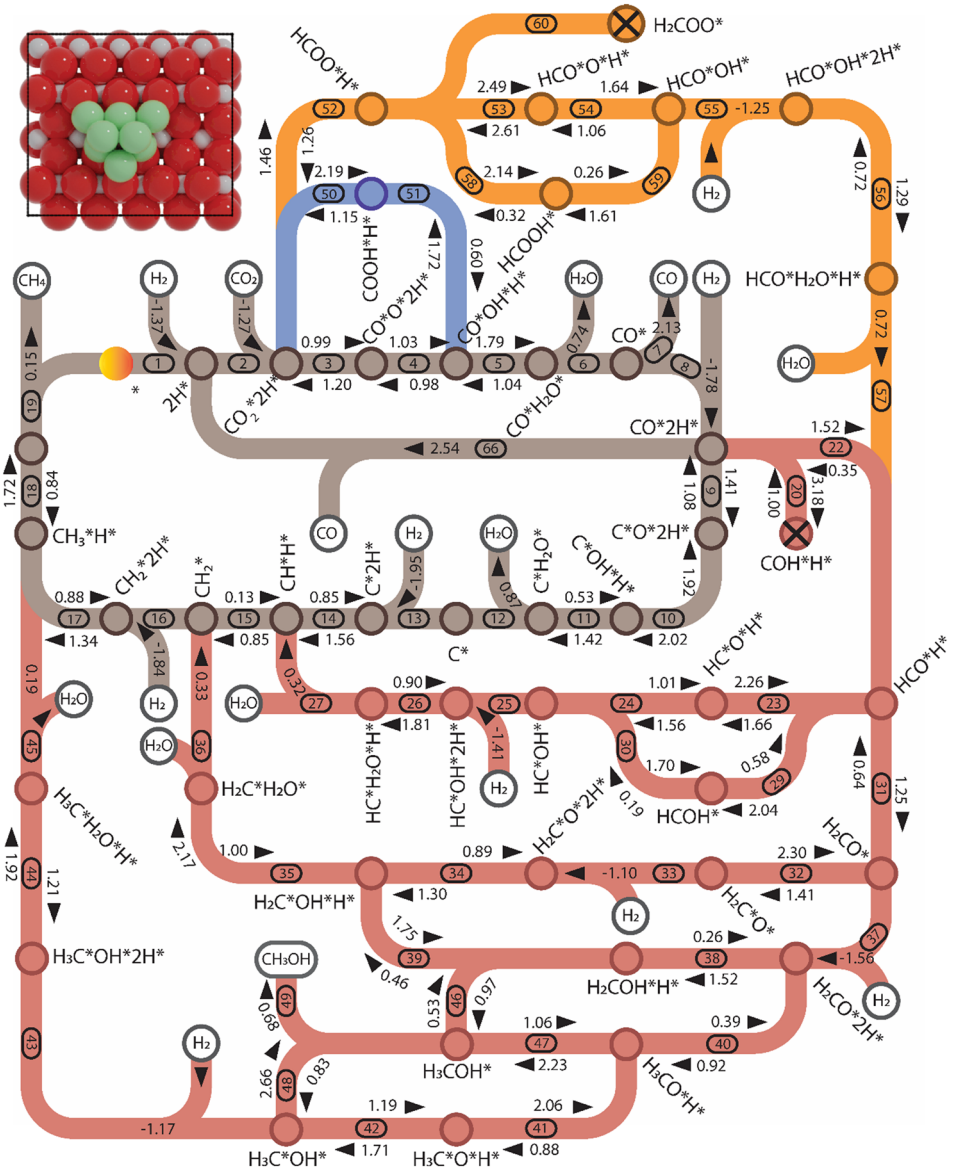

Fig. 6 The forward and backward activation energies in the network of CO_2 hydrogenation in C_1 chemistry for Ni_8-TiO_2-r (colors: brown: CH_x-intermediates pathway; red: H_xCO-intermediates pathway; and orange and blue: H_xCOO-intermediates pathways). The energy reported here is zero-energy corrected and given by eV. The cross on COH*H* and H_2COO* signifies that their formation is impeded by high activation energies, leading to the exclusion of subsequent reactions. The numbers correspond to the elementary reaction steps in Table S1 and S2 and Fig. S12–S15.† The activation energy, adsorption energy, and desorption energy are reported in eV and include a zero-point energy correction.

emphasized that CO desorption can also occur at the states CO*O*2H*, CO*OH*H* and CO*2H* with desorption energies of 2.18, 2.16 and 2.17 eV, respectively. These pathways are not explicitly shown in Fig. 5, though they are taken into account in the microkinetic modelling (*vide infra*).

The adsorption of H_2 on the surface containing CO* (R8) is exothermic by −1.46 eV. The direct dissociation of CO* (R9, ΔE_{act} = 1.99 eV, ΔE_R = −0.24 eV) generates an adsorbed C* at $F_{1\text{–}2\text{–}7\text{–}8}$ site and an adsorbed O* at $H_{5\text{–}6\text{–}7}$ site, which can be hydrogenated to CH_4 and H_2O, respectively. Compared to the direct CO dissociation on Ni_8/In_2O_3 (ΔE_{act} = 3.24 eV),[62] which shares a similar Ni_8 cluster morphology as Ni_8/TiO_2 anatase, a lower activation energy is observed on Ni_8/TiO_2 anatase. This suggests that Ni/TiO_2 is a more effective catalyst for CO_2 methanation than Ni/In_2O_3, the latter mainly producing methanol. In contrast, the work of Sterk *et al.*[65] shows that for the Ni(110) extended surface a relatively low barrier of ΔE_{act} = 1.56 eV is found for CO dissociation. Hydrogenation of O* to OH* (R10) is endothermic by 0.60 eV with an activation energy of 1.52 eV. The OH* reacts with another H* to form an H_2O molecule (R11, ΔE_{act} = 1.46 eV, ΔE_R = 1.03 eV), which then desorbs from the surface (R12, ΔE_{des} = 0.74 eV) and leaves an adsorbed C* species. H_2 adsorption (R13) provides two H* with an adsorption energy of −1.60 eV. C* is subsequently hydrogenated to CH* (R14, ΔE_{act} = 0.88 eV, ΔE_R = 0.39 eV) and CH_2^* (R15, ΔE_{act} = 0.97 eV, ΔE_R = 0.70 eV). In

order to form CH_4, one more H_2 molecule adsorbs (R16, ΔE_{ads} = −1.86 eV). The reaction between CH_2^* and H* results in the formation of CH_3^* (R17, ΔE_{act} = 1.31 eV, ΔE_R = 0.49 eV). Next, H* migrates from B_{6-7} to H_{1-6-7} resulting in a more stable configuration (ΔE_R = −0.31 eV). This H* reacts with CH_3^* forming CH_4^* (R18) with an activation energy of 1.41 eV and this step is endothermic by 0.74 eV. The final step is CH_4 desorption (R19) closing the catalytic cycle.

Pathway involving H_xCO intermediates. For many transition metals, it has been observed that when direct C–O bond scission is associated with a prohibitively high barrier, CO dissociation will occur *via* COH* or HCO* intermediates.[65] These steps correspond to the red section in Fig. 5. Starting at co-adsorbed CO and H_2 (between R8 and R9), CO* can become hydrogenated to COH* (R20) with an activation energy of ΔE_{act} = 2.27 eV (ΔE_R = 1.38 eV). Its subsequent dissociation (R21, ΔE_{act} = 1.10 eV, ΔE_R = −1.05 eV) results in the same configuration of C*OH*H* as found in the direct CO* dissociation pathway. The overall activation energy for COH* dissociation is 2.48 eV, which is higher than the activation energy for the direct CO* dissociation. The alternative pathway proceeds *via* the hydrogenation of CO* to form HCO* (R22), which is endothermic by 1.06 eV and has an activation energy of 1.16 eV. Next, the H* located at H_{3-4-8} migrates to a more stable site (B_{6-7}) with an exothermic reaction energy of 0.33 eV. HCO* dissociation generates an adsorbed CH* and O* (R23, ΔE_{act} = 0.93 eV, ΔE_R = −0.79 eV). The overall activation energy for the HCO* formation and dissociation is 1.66 eV, lower than the overall barriers found for direct CO* dissociation and COH* pathways, corresponding to 1.99 and 2.48, respectively. The overall activation energy of 1.66 eV lies in between the values found for Ni_8/In_2O_3 (1.80 eV)[62] and for a stepped Ni(110)[65] surface (1.21 eV).

After HCO* dissociation, the O* reacts with the remaining H* forming OH* (R24). The activation energy and reaction energy for OH* formation are ΔE_{act} = 1.84 eV and ΔE_R = 0.67 eV, respectively, including the migration of H* and OH*. H_2 adsorption provides two H* located at H_{1-6-7} and H_{3-4-8} (R25, ΔE_{ads} = −1.28 eV). The OH* then is hydrogenated to H_2O* (R26, ΔE_{act} = 1.05 eV, ΔE_R = 0.81 eV), which desorbs from the surface (R27) and generates the same configuration of CH*H* as found in the direct CO dissociation pathway.

Alternatively, HCO* can be hydrogenated to form HCOH* (R29, ΔE_{act} = 2.28 eV, ΔE_R = 0.99 eV), which can alternatively be obtained through COH* hydrogenation (R28, ΔE_{act} = 1.25 eV, ΔE_R = 0.64 eV). HCOH* dissociation yields HC* and OH* (R30) with an activation energy of 0.95 eV and a reaction energy of −1.43 eV. The overall activation energies of HCOH* dissociation *via* COH* and HCO* are 2.97 eV and 2.98 eV, respectively. Both these pathways are higher in energy than the overall activation energy of HCO* dissociation, implying that the HCOH* dissociation pathway is unlikely to occur.

Another mode of H-assisted CO dissociation proceeds *via* the hydrogenation of HCO* to form H_2CO* which can subsequently dissociate (R31 and R32). These two steps require activation energies of 1.19 eV and 2.19 eV, respectively. The corresponding reaction energies are 0.63 eV and −0.60 eV. The overall activation energy from CO*2H* to H_2C*O* is 3.52 eV, implying that this pathway is likely not the most favorable pathway. H_2 adsorption (R33, ΔE_{ads} = −1.32 eV) provides two H* to remove the O* through the formation of H_2O. The reaction starts with the interaction of O* and H* (R34, ΔE_{act} = 1.10 eV, ΔE_R = 0.04 eV), leading to the formation of OH* which can be further hydrogenated to H_2O* (R35, ΔE_{act} = 1.99 eV, ΔE_R = 1.42 eV). Finally, H_2O desorbs from the catalyst surface (R36, ΔE_{des} = 0.70 eV), leaving behind CH_2^* as an adsorbate on the catalyst surface and linking back to the CH_x-intermediates section of the kinetic network.

CH_3OH formation can proceed *via* twofold hydrogenation of H_2CO*. Two H* are supplied by the adsorption of H_2 (R37, ΔE_{ads} = −1.23 eV) after which H_2CO* can be hydrogenated to form H_3CO* (R40, ΔE_{act} = 0.91 eV, ΔE_R = 0.53 eV). The H_3CO* intermediate can be further hydrogenated to form adsorbed CH_3OH (R47, ΔE_{act} = 1.80 eV, ΔE_R = 0.87 eV) or dissociate into H_3C* and O* (R41, ΔE_{act} = 0.75 eV, ΔE_R = −0.25 eV), the latter being clearly more favorable. The dissociated O* combines with the H* forming OH* (R42) with an activation energy of 0.34 eV. Alternatively, this state can also be obtained *via* H_3COH* dissociation (R48, ΔE_{act} = 0.55 eV, ΔE_R = −1.70 eV). H_2 adsorption on the surface containing CH_3^* and OH* (R43) is exothermic by 1.34 eV. The resulting H* atoms can hydrogenate OH* forming H_2O (R44, ΔE_{act} = 1.66 eV, ΔE_R = 0.38 eV) which can desorb from the surface with a desorption energy of 1.05 eV (R45) leaving CH_3^* and H*.

The last branch in the H_xCO* section of the kinetic network involves the conversion of the O-terminated H_2CO* intermediate. H_2CO* can be hydrogenated to form H_2COH* (R38, ΔE_{act} = 1.58 eV, ΔE_R = 0.82 eV) which in turn can dissociate into H_2C* and OH* (R39) with an activation energy of 0.52 eV. This step is exothermic by 1.46 eV. Alternatively, H_2COH* is hydrogenated to H_3COH* (R46), which is associated with an activation energy of 0.93 eV and an endothermic reaction energy of 0.58 eV.

3.2.2.2 Ni_8/TiO_2-r

Pathway involving CH_x intermediates. The brown section in Fig. 6 corresponds to the elementary reaction steps among the CH_x intermediates over Ni_8/TiO_2-r. After adsorption of H_2 (R1) and CO_2 (R2), direct dissociation of CO_2^* generates adsorbed CO* and O* (R3, ΔE_{act} = 0.99 eV, ΔE_R = −0.21 eV). The dissociated O* atom is removed by H* through the formation and desorption of H_2O. The formation of OH* (R4), including a migration of O* from H_{2-7-8} to H_{2-3-8}, requires and activation energy of 1.03 eV and is endothermic by 0.25 eV. To facilitate the formation of H_2O, the remaining H* needs to migrate to the H_{2-3-8} site to be close to the OH* (ΔE_R = 0.54 eV). The activation energy and reaction energy for H_2O* formation (R5) are 1.25 eV and 0.21 eV, respectively. Finally, the desorption of H_2O (R6) is endothermic by ΔE_{des} = 0.74 eV, leaving an adsorbed CO* on Ni_8/TiO_2-r. This remaining CO* species can either desorb from the surface (R7) with a desorption energy of ΔE_{des} = 2.13 eV or dissociate to form C* and O*. Similar to the Ni_8/TiO_2-a system, CO desorption can also occur at the states CO*O*2H*,

CO*OH*H* and CO*2H* with desorption energies of 2.11, 2.23 and 2.54 eV, respectively. These pathways are not explicitly shown in Fig. 6, though they are taken into account in the microkinetic modelling (*vide infra*).

The adsorption of H_2 on the surface containing CO* (R8) is exothermic by 1.78 eV. It is important to note that CO can desorb from CO*2H*, generating 2H* species (R66, ΔE_{des} = 2.54 eV), which should be considered as a part of the rWGS cycle. A relatively low activation energy of 1.41 eV is required for direct CO* dissociation (R9, ΔE_R = 0.33 eV). The dissociated O* fragment is two-fold hydrogenated to form H_2O. After the formation of OH* (R10, ΔE_{act} = 2.02 eV, ΔE_R = 0.80 eV), the OH* migrates from $H_{2\text{–}7\text{–}8}$ to $B_{7\text{–}8}$ (ΔE_R = −0.70 eV). Subsequently the OH* reacts with the remaining H* forming H_2O* (R11, ΔE_{act} = 1.42 eV, ΔE_R = 0.89 eV). After the desorption of H_2O (R12, ΔE_{des} = 0.87 eV), the C* undergoes four consecutive hydrogenation steps yielding CH_4. H_2 adsorption (R13, ΔE_{ads} = −1.95 eV) provides two H* for the hydrogenation of C* to CH* (R14, ΔE_{act} = 1.56 eV, ΔE_R = 0.71 eV) and CH_2^* (R15, ΔE_{act} = 0.85 eV, ΔE_R = 0.75 eV). CH_2^* will be hydrogenated to CH_3^* and CH_4^* by the presence of two H* (R16, ΔE_{ads} = −1.84 eV). CH_3^* formation (R17) is endothermic by 0.47 eV overcoming an activation energy of 1.34 eV. CH_3^* migration from $T_{6\text{–}7\text{–}8}$ to $B_{7\text{–}8}$ (ΔE_R = 0.02 eV) is followed by the formation of CH_4. The activation energy and reaction energy for CH_4 formation (R18) are 1.72 eV and 0.86 eV, respectively. Once CH_4 is formed, it desorbs from the catalyst (R19, ΔE_{des} = 0.15 eV).

Pathway involving H_xCO intermediates. In the red section of Fig. 6, the elementary reaction steps involving H_xCO species are shown. Part of this network is comprised of the H-assisted CO dissociation. Due to the high activation energy required to form COH* formation (R20, ΔE_{act} = 3.18 eV), we did not proceed with the calculation of the subsequent COH* dissociation or COH* hydrogenation to HCOH*. The alternative route for CO* hydrogenation by C–H bond formation leading to HCO* (R22) has an activation energy of 1.52 eV and is endothermic by 1.17 eV. Subsequent dissociation of HCO* (R23) results in the formation of CH* located at $H_{6\text{–}7\text{–}8}$ and O* located at $H_{1\text{–}4\text{–}7}$. The activation energy and reaction energy associated with the dissociation of HCO* are 1.66 eV and −0.60 eV, respectively. Due to the large distance between O* and H*, H* needs to migrate to $H_{1\text{–}2\text{–}7}$ site first (ΔE_R = 0.35 eV). Formation of OH* (R24) requires an activation energy of 1.21 eV, accompanied by a reaction energy of 0.20 eV. H_2 adsorption (R25) provides H* to hydrogenate the OH* to H_2O* and is associated with an adsorption energy of −1.41 eV. OH* reacts with H* located at $H_{2\text{–}7\text{–}8}$ forming H_2O (R26, ΔE_{act} = 1.81 eV, ΔE_R = 0.91 eV), which desorbs generating CH*H* (R27, ΔE_{des} = 0.32 eV), linking back to the CH_x-intermediates section. HCO* can be hydrogenated to HCOH* (R29) by overcoming an activation energy of 2.04 eV. The formation of HCOH* is endothermic by 1.46 eV. HCOH* can be dissociated into CH* and OH* (R30) with an activation energy of ΔE_{act} = 0.19 eV and a reaction energy of ΔE_R = −1.51 eV.

HCO* can undergo hydrogenation to form H_2CO* (R31, ΔE_{act} = 1.25 eV, ΔE_R = 0.61 eV), which then dissociates into H_2C* and O* by overcoming an activation energy barrier of 1.41 eV (R32). The dissociation of H_2CO* is exothermic by 0.89 eV. The O* species is subsequently hydrogenated to H_2O*. The adsorption of H_2 on the surface containing H_2C* and O* is exothermic by 1.10 eV (R33). The initial hydrogenation of O* leads to the formation of OH* (R34), involving an activation energy of 1.30 eV and a reaction energy of 0.40 eV. The migration of H* occurs to react with OH* and form H_2O (ΔE_R = 0.52 eV). Subsequently, the formation of H_2O (R35) is endothermic by 0.65 eV, requiring an activation energy of 1.65 eV. Finally, H_2O desorbs into the gas phase (R36) with a reaction energy of 0.33 eV and leaving an adsorbed CH_2^* species on the surface. The subsequent hydrogenation of CH_2^* to CH_4 has been discussed in the CH_x^* intermediates pathway (*vide supra*).

The adsorption of H_2 on the surface containing H_2CO* provides two H* species, which are subsequently utilized for the hydrogenation of H_2CO*. This adsorption process is exothermic by 1.56 eV (R37). Hydrogenation of H_2CO* can occur either *via* hydrogenation at the O-terminus or at the C-terminus, resulting in the formation of H_2COH* (R38, ΔE_{act} = 1.52 eV, ΔE_R = 1.27 eV) or H_3CO* (R40, ΔE_{act} = 0.92 eV, ΔE_R = 0.53 eV), respectively. The dissociation of H_2COH* gives rise to H_2C*OH*H* (R39, ΔE_{act} = 0.46 eV, ΔE_R = −1.29 eV), which serves as an intermediate in the H_2CO* dissociation pathway. H_3CO* resulting from H_2CO* hydrogenation can either undergo another hydrogenation step to form H_3COH* (R47) or dissociate into H_3C* and O* (R41). The dissociation of H_3CO* is more favorable, exhibiting an activation energy of ΔE_{act} = 0.88 eV and is exothermic by ΔE_R = −1.17 eV. In comparison, its hydrogenation has an activation energy of ΔE_{act} = 2.23 eV and a reaction energy of ΔE_R = 1.18 eV. Upon the dissociation of H_3CO*, the O* reacts with the remaining H* forming OH* (R42, ΔE_{act} = 1.71 eV, ΔE_R = 0.52 eV). This configuration can alternatively be obtained through the dissociation of the C–O bond in H_3COH* (R48, ΔE_{act} = 0.83 eV, ΔE_R = −1.83 eV). The OH* is hydrogenated to H_2O* in the presence of H* (R44, ΔE_{act} = 1.92 eV, ΔE_R = 1.21 eV). The H* is provided by the adsorption of H_2 (R43), which is exothermic by 1.17 eV. Finally, H_2O desorbs from the surface with a desorption energy of 0.19 eV (R45). On the surface, there exist a CH_3^* species along with a remaining H* species, and the reaction between these two entities has been previously described within the context of the CH_x^* intermediates pathway. Finally, hydrogenation of H_2COH* leads to the formation of H_3COH* with an activation energy of 0.97 eV and a reaction energy of 0.44 eV (R46), which can desorb from the surface (R49, ΔE_{des} = 0.68 eV).

3.2.2.3 Comparison of reaction networks. Overall, our investigations on both Ni_8/TiO_2-a and Ni_8/TiO_2-r surfaces indicate that the direct dissociation of CO_2 is favored over H-assisted CO_2 dissociation. The corresponding reaction energy diagrams for this pathway is shown in Fig. S16.† This finding aligns with the observations made by Zhang *et al.*,

who conducted DFT calculations on Ni_4/CeO_2 (111) and reported activation energies of 2.55 eV for HCOO* formation, 2.80 eV for COOH* formation, and 1.60 eV for CO_2 direct dissociation.[66]

The activation energy for the direct dissociation of CO* on Ni_8/TiO_2-a is 1.88 eV. In comparison, the overall activation energy for HCO* formation and dissociation is 1.66 eV whereas the overall activation energy for H_2CO* formation *via* CO*2H* → HCO*H* → H_2CO* is 1.92 eV. Based on these values, the H-assisted CO* dissociation *via* HCO* is energetically the most favorable pathway. For Ni_8/TiO_2-r, it was found that direct dissociation of CO* requires an activation energy of 1.41 eV. In comparison, the overall activation energy for HCO* formation and dissociation is 2.83 eV while the overall activation energy for H_2CO* formation is 2.42 eV. Based on these numbers, direct CO* dissociation is energetically the most likely pathway over Ni_8/TiO_2-r.

Finally, comparing Ni_8/TiO_2-r to Ni_8/TiO_2-a, the former exhibits a lower activation energy for the direct dissociation of CO*, but the subsequent hydrogenation steps are associated with higher barriers. For example, the overall activation energy for CH_2^* hydrogenation to CH_4 on Ni_8/TiO_2-a and Ni_8/TiO_2-r are 1.59 eV and 2.18 eV, respectively. Nevertheless, assessment of the most facile pathways purely based on the DFT energetics remains in absence of the surface coverages limited and microkinetics simulations are conducted to further study the kinetic behavior of these systems.

3.3 Microkinetics simulations

Microkinetics simulations are conducted to predict the catalytic performance of Ni_8/TiO_2-a and Ni_8/TiO_2-r for CO_2 hydrogenation. The activation energies and pre-exponential factors as determined by DFT were employed for these microkinetics simulations.

Fig. 7 depicts the reaction rate and product distribution for Ni_8/TiO_2-a and Ni_8/TiO_2-r. Ni_8/TiO_2-a exhibits a significantly higher CO_2 conversion rate than Ni_8/TiO_2-r. These turn-over-frequencies are lower than those observed by Liu *et al.*, who report a TOF = 2.14×10^{-3} for Ni nanoparticles of 2.2 nm at a temperature of T = 200 °C.[67] Abir *et al.* reported a TOF = 2×10^{-2} for 2.9 nm particles at T = 350 °C.[68] In both studies, a mixed anatase/rutile support was used. In contrast, Li *et al.* report a TOF = 5.1×10^{1} s^{-1} for 1 nm particles supported on TiO_2-anatase at T = 500 °C.[69] These latter results align well to our results found for Ni_8/TiO_2-a. At low temperature, both surface models produce mainly CH_4, while the selectivity to CO increases with temperature at the expensive of the CH_4 selectivity. The selectivity towards CH_3OH is negligible at all temperatures considered. At a temperature of 350 K, Ni_8/TiO_2-a only produces CH_4, while the CH_4 selectivity for Ni_8/TiO_2-r is 85%.

To determine the dominant pathway for CO_2 hydrogenation within the chemokinetic network of Ni_8/TiO_2-a and Ni_8/TiO_2-r, a reaction pathway analysis is conducted. Fig. S17 and S18† provide the molar rate fluxes for Ni_8/TiO_2-a and Ni_8/TiO_2-r at T = 600 K. The dominant reaction pathways for product formation at this temperature are indicated in Fig. 8. For both models, direct dissociation of CO_2 is preferred over H-assisted CO_2 dissociation. The manner of CO dissociation differs between Ni_8/TiO_2-a and Ni_8/TiO_2-r. On Ni_8/TiO_2-a, the former favors H-assisted CO dissociation while the latter favors direct CO* dissociation.

To determine which steps control the overall activity and selectivity, DRC and DSC analyses (with respect to CO_2 consumption) are conducted. Fig. 9a shows that at low temperature, the desorption of H_2O (R6 in Fig. 5) is the rate-determining step on Ni_8/TiO_2-a. The dominant species on the surface is CO*O*2H* (Fig. 9b). This observation can be attributed to the fact that the elementary reactions R4, R5, and R6 in Fig. 5 are endothermic. As such, CO*O*2H* is the state lowest in energy prior to the rate-determining step R6 which consequently becomes the most abundant state under these conditions. From Fig. 9c, we can see that the apparent activation energy is around 200 kJ mol^{-1} at low temperature and decreases with increasing temperature. This result can be rationalized from Fig. 9g which shows the potential energy diagram for CH_4 formation *via* the HCO* dissociation pathway. The dominant intermediary state is highlighted in

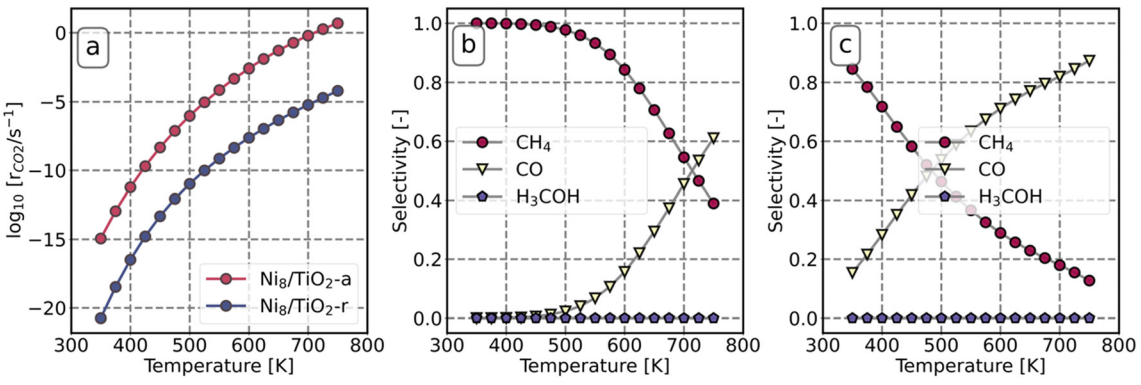

Fig. 7 Reaction rate of CO_2 as a function of temperature (a). The selectivity of CO, CH_4 and H_3COH as a function of temperature on Ni_8/TiO_2-a (b) and Ni_8/TiO_2-r (c).

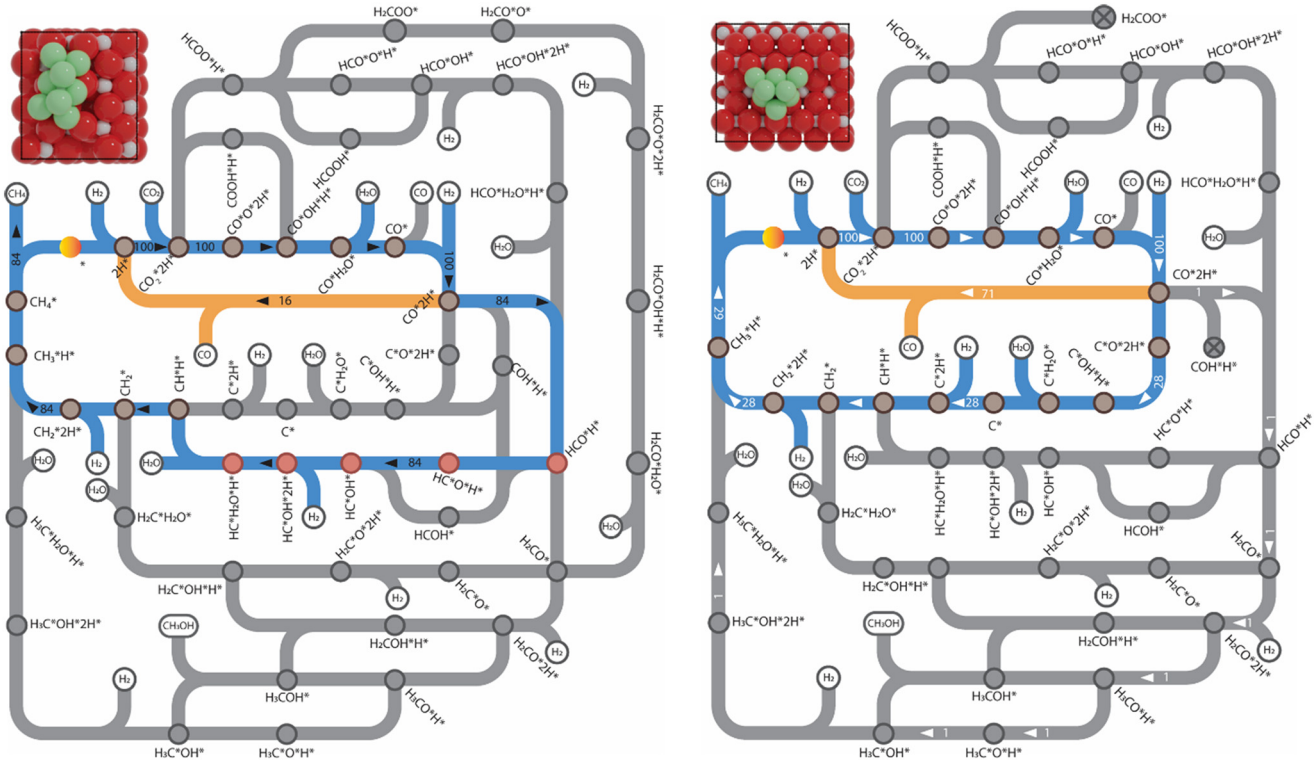

Fig. 8 Preferred pathways for CO_2 hydrogenation on Ni_8/TiO_2-a (left) and Ni_8/TiO_2-r (right). The production of CO and CH_4 is represented by the yellow and blue paths, respectively. All values are normalized with respect to the rate of adsorbed CO_2 and are given in percentages (%).

red and the overall barrier for H_2O desorption (the rate-determining step) with respect to this state is determined to be 2.08 eV, which is in agreement with the apparent activation energy. The reaction orders are in line with this observation. Since the dominant CO*O*2H* state already has two hydrogen atoms present, no further hydrogen is necessary to proceed towards the rate-determining step and consequently the reaction order in H_2 (Fig. 9c) is observed to be zero. Likewise, since the dominant state already represents the fragments of CO_2 dissociation, a reaction order of 0 in CO_2 is found.

At temperatures between T = 500 K and T = 650 K, H_2O desorption becomes less rate-limiting to the rate of CO_2 consumption while HCO*H* ⇄ HC*O*H* (R23) and CH_3^* hydrogenation (R18) becomes more rate-limiting. Simultaneously, it is observed that CO desorption (R66) becomes rate-inhibiting. Due to the increase in temperature, there is more thermal energy available to overcome the H_2O desorption barrier resulting in barriers further down the kinetic pathway to become rate-limiting. Since CO desorption (R66) prevents the formation of CH_4 which is still the dominant product under these conditions, this step is rate-inhibiting. Further increasing the temperature above T = 650 K results in further decreasing the degree of rate control of the H_2O desorption reaction. Simultaneously, HCO*H* ⇄ HC*O*H* (R23) becomes rate-inhibiting, whereas CH_3^* hydrogenation (R18) and CO desorption (R66) become rate-limiting. These changes reflect the change in selectivity from CH_4 to CO. At elevated temperature, the dominant pathway switches from CH_4 production *via* the HCO* intermediate to a rWGS pathway *via* R66. Since H_2O desorption is a step in the kinetic network for both CO as well as CH_4 production, this step remains rate-limiting to some extent. CH_3^* hydrogenation is also still a rate-limiting step as even at elevated temperature there remains a significant selectivity towards CH_4. Nevertheless, the rate of CO_2 consumption for CH_4 production is lower than for CO and a change in selectivity towards CH_4 by lowering the barrier for HCO*H* ⇄ HC*O*H* would result in a decreased overall activity, explaining why this step becomes rate-inhibiting at elevated temperature. The DSC analysis as shown in Fig. S19† further reflects upon this. From this figure, it can be seen that HCO*H* ⇄ HC*O*H* and CO* desorption control the selectivity between CH_4 and CO. The apparent activation energy and reaction orders change accordingly as a function of temperature. With increasing temperature, the catalyst tends to reside in states further down the kinetic pathway with respect to CO*O*2H*, specifically CO*OH*H*, CO*2H*, C*O*2H*, C*2H* and CH_2^*2H*. From Fig. 9f it can be readily seen that these states are all higher in energy with respect to CO*O*2H*. With respect to the barrier of the dominant rate-limiting step for these intermediates, *i.e.* either CH_3^* hydrogenation or CO* desorption, the energy difference is somewhat smaller than between CO*O*2H* and the barrier for H_2O^* desorption. Since all these intermediary species already contain fragments arising from CO_2^* adsorption, the

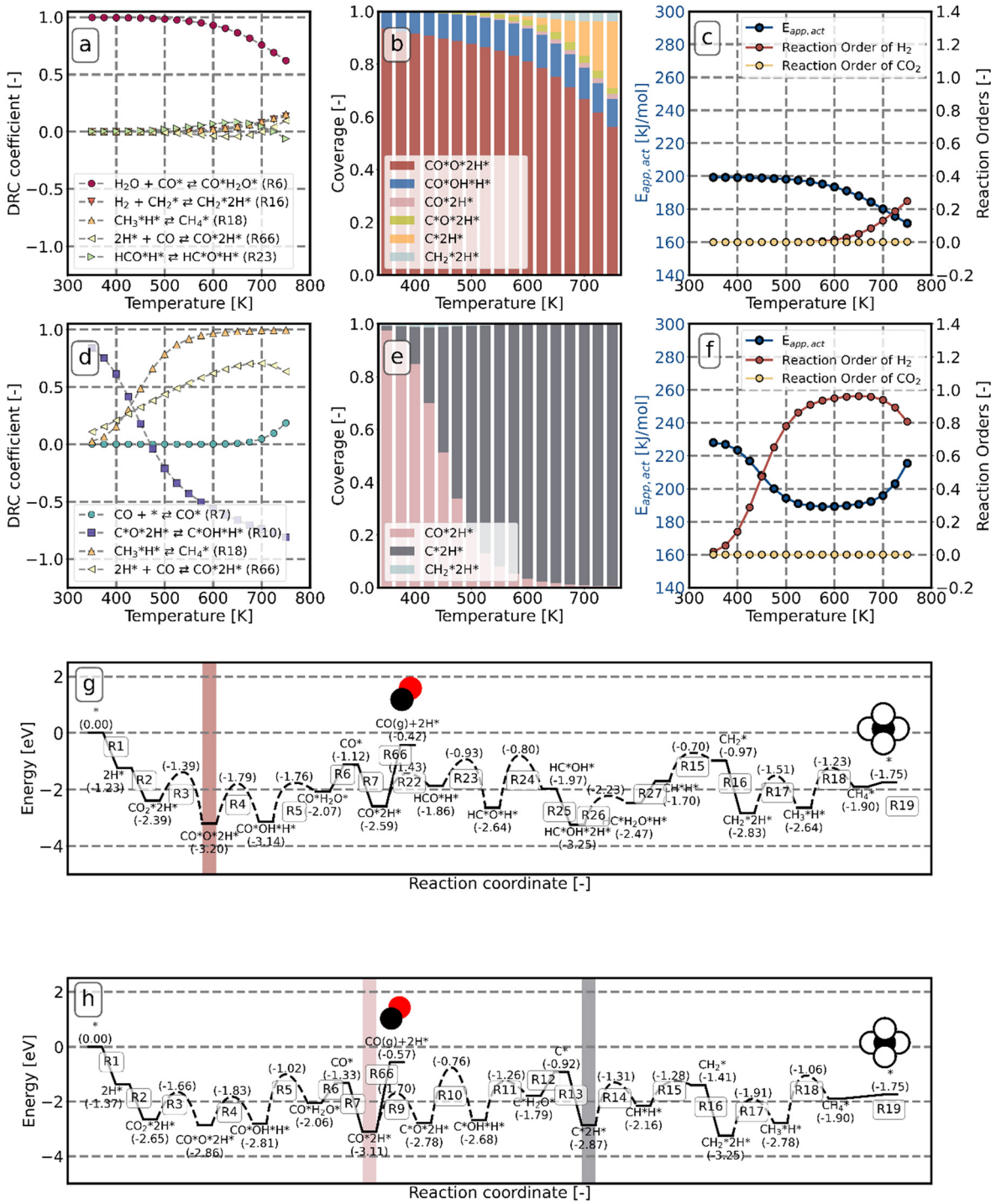

Fig. 9 Degree of rate-control coefficient with respect to CO_2 consumption (a and d), the steady state of surface coverage (b and e), the apparent activation (c and f), the reaction orders of CO_2 and H_2 (c and f) as a function of temperature. Ni_8/TiO_2-a: a–c; Ni_8/TiO_2-r: d–f. The potential energy diagram of CO_2 methanation on Ni_8/TiO_2-a (g) and Ni_8/TiO_2-r (h). In figures (g) and (h), the predominant species are accentuated using consistent color coding in the coverage plots.

reaction order in CO_2 remains zero. In contrast, with the exception of $CH_2^*2H^*$, all other abundant intermediary states require the adsorption of another H_2 molecule in order to proceed to the rate-limiting step of CH_3^* hydrogenation. Consequently, the increased reaction order in H_2 reflects the decrease in surface abundance of CO*O*2H* in favor of a number of intermediates that are precursor species towards CH_4 formation that requires the adsorption of H_2 to produce CH_4.

In Fig. 9d, the DRC analysis for Ni_8/TiO_2-r is shown. At low temperatures, the reaction is mainly controlled by the rate of C*O*2H* ⇄ C*OH*H* (R10) and CO*2H* is the most

abundant cluster configuration. The desorption of CO requires 2.54 eV, whereas the activation energy between CO*2H* and R10 is 2.35 eV. At low temperature CH_4 formation is preferred, yet the selectivity towards CH_4 rapidly decreases in favor of CO with increasing temperature as desorption rates increase more rapidly with increasing temperature in comparison to surface reactions. With increasing temperature, the degree of rate-control of step R10 decreases in favor of CO* desorption (R66) and CH_3 hydrogenation (R18) becoming rate-limiting steps. A further increase in temperature results in C*O*2H* ⇄ C*OH*H* becoming rate-inhibiting while the degree of rate-control for CO* desorption and CH_3 hydrogenation increase further. From Fig. 9e, it is found that CO*2H is the dominant surface state at the low temperature regime whereas with increase in temperature C*2H* becomes the most abundant surface state. The change in surface coverage reflects the degree of rate control for C*O*2H* ⇄ C*OH*H*. When this step is rate-controlling, the state lowest in energy prior to the barrier of this step corresponds to CO*2H*. When this step is no longer rate-limiting due to the increase in temperature, the state C*2H* is the next state lowest in energy prior to one of the rate-limiting steps (*i.e.* R18 and R66).

The apparent activation energy and the reaction orders as shown in Fig. 9f are in line with these trends. At low temperature, a value of 230 kJ mol^{-1} is found, corresponding to the difference in energy between the CO*2H state (Fig. 9h, highlighted in pink) and the height of the transition state for C*O*2H hydrogenation. With increasing temperature, the system spends more time in the C*2H* state which lies higher in energy. Consequently, the apparent activation energy decreases. In contrast to the low temperature situation, a facile quantitative comparison between the energy levels of the states in the potential energy diagram and the apparent activation energy is not possible for the high temperature situation as no single elementary reaction step is predominantly rate-controlling. The increase in the apparent activation energy for $T > 700$ K is caused by the deposition of carbonaceous species leading to catalyst deactivation. The observation that C*O*2H* hydrogenation is strongly rate-inhibiting is in line with this observation. As this step becomes more facile, O* that could otherwise be used to recombine with C* to form CO* which can desorb from the surface, is now removed as H_2O. In absence of O* and with C* + 2H* being very stable on the surface, further progression towards CH_4 is prevented. The branch in the kinetic network *via* R9–R13 effectively leads to a dead state of the catalyst. Finally, Fig. 9f shows that the reaction order in CO_2 remains close to zero, irrespective of temperature whereas the reaction order in H_2 increases as a function of temperature. Since both the CO*2H* intermediate and the C*2H* intermediates already contain the dissociation fragments of CO_2 necessary for the rate-limiting steps to proceed, an increase or decrease in the partial pressure of CO_2 will not affect the overall rate. In contrast, in the high temperature regime the dominant state lacks 2H* species for the CH_3^* + H* reaction to proceed. The reaction order in H_2 therefore reflects the extent to which this pathway controls the overall reaction rate. At temperatures $T > 700$ K, we however observe that the reaction order in H_2 slightly decreases. Here, additional H* is detrimental to the activity of the catalyst as it leads to further O* removal and thus the formation of strongly bound C*.

Conclusively, the lower reactivity observed for the Ni_8/TiO_2-r system in comparison to Ni_8/TiO_2-a is caused by the presence of a relative facile direct CO dissociation. The low barrier for CO dissociation coincides with C* being strongly bound to the catalyst leading to catalyst deactivation. In contrast, for Ni_8/TiO_2-a, direct CO dissociation is difficult, and a H-assisted pathway is more facile. This is already indicative for C* being less strongly bound to the catalyst benefiting its activity. These results are according to the Sabatier principle which shows that although strong adsorption leads to facile activation of the adsorbates, it prevents the desorption of the products, poisoning the catalyst.

As the utilization of the PBE functional commonly leads to an overestimation of the binding energy of CO,[70–72] we need to critically assess its effect. As such, additional microkinetic simulations were conducted wherein simultaneously the CO and CO_2 adsorption energy were decreased in a range of 0.0 to 0.3 eV on both Ni_8/TiO_2-a and Ni_8/TiO_2-r models, ensuring that this modification does not affect the overall thermodynamics of the reaction. The resulting reaction rates of CO_2 and selectivity were analyzed and summarized in Fig. S26 and S27.† Decreasing the CO adsorption energy on both Ni_8/TiO_2-a and Ni_8/TiO_2-r catalysts results in an increase in the CO selectivity. For these two surfaces, CO becomes the main product when the correction of CO adsorption energy was set to 0.3 eV at 600 K.

Although we established that H-spillover is associated with relatively high barriers, we nevertheless explored the effect of an enhanced H* coverage on the Ni_8-clusters. This analysis was however limited to CO and HCO dissociation and HCO formation as these steps were found to affect the selectivity of the reaction (Fig. S19†). As we determined H-spillover to be difficult, thus assuming that accumulation of additional H* species on the clusters would proceed *via* adsorption from the gas phase, we furthermore calculated the adsorption energy of H_2 as function of the H* coverage. The results are shown in Tables S3–S5 in the ESI.† From Tables S3 and S4,† it can be seen that on Ni_8/TiO_2-anatase, the overall activation energies for HCO* formation and dissociation are always higher than the activation energies for direct dissociation of CO*. Conversely, on the Ni_8/TiO_2 rutile surface, the direct CO* dissociation exhibits a lower activation energy as compared to the HCO* formation and dissociation. Therefore, the conclusion that Ni_8/TiO_2 anatase predominantly follows the HCO* pathway while Ni_8/TiO_2-rutile favors the direct CO* dissociation pathway remains valid, irrespective of the H* coverage. Furthermore, from Table S5† it can be observed that additional H* accumulation is associated with a significantly decreased

adsorption energy. Given the loss of entropy of H_2 upon adsorption, we estimate, especially at higher temperature, that the presence of more than two H* species, in addition to H_xCO, on the Ni_8 clusters is highly unlikely.

From these additional simulations we can conclude that the Ni_8 clusters have a vastly lower activity as compared to experiment,[67,68] even when taking potential effects of overbinding and H-accumulation into account. Despite that Ni_8/TiO_2-r allows for a direct CO dissociation, it results in the formation of a very stable C* species effectively poisoning the catalyst surface. This poisoning condition is less severe on Ni_8/TiO_2-a, yet compared to extended Ni surfaces, also here much higher adsorption energies are observed for the reaction intermediates. We assign the increased adsorption strength of CO* and C* to the presence of coordinatively undersaturated Ni atoms in these clusters, which due to the specific alignment of the Ni atoms with the support, lead to much stronger adsorption energies for Ni_8/TiO_2-rutile as compared to Ni_8/TiO_2-anatase.

3.4 Electronic structure analysis

Microkinetic simulations show that for both Ni_8/TiO_2-a as well as Ni_8/TiO_2-r the initial C–O bond scission in CO_2 proceeds in a direct fashion. After removal of the dissociated O* fragment as H_2O, the remaining CO* fragment needs to dissociate as well for CH_4 formation. For this step, the two models differ in the preferred pathway as shown in Fig. 8. For Ni_8/TiO_2-a, C–O bond scission proceeds in a H-assisted fashion *via* an HCO* intermediate, whereas for Ni_8/TiO_2-r it proceeds in a direct fashion. This observation can be readily explained based on the activation energies. The activation energy of CO direct dissociation for Ni_8/TiO_2-r is 1.41 eV, whereas for Ni_8/TiO_2-a a higher activation energy of 1.99 eV is found. The barriers for CO* hydrogenation to HCO* and its subsequent dissociation to CH* and O* are 1.16 eV and 0.93 eV. Despite the initial hydrogenation step being endothermic by 0.70 eV, the effective barrier for the H-assisted step is 1.66 eV, making the H-assisted pathway preferred over the direct pathway.

To better understand the differences in the activation energies of CO* direct dissociation, we performed a density of states (DOS) and Crystal Orbital Hamilton Population (COHP) analysis on CO* and the transition state of its dissociation towards C* + O* for Ni_8/TiO_2-a and Ni_8/TiO_2-r. The results of this analysis are shown in Fig. 10 and S24.† In Fig. S21a and f,† the DOS and COHP for the C–O interaction of CO in the gas phase is shown. Note that a more negative COHP coefficient indicates that the Kohn–Sham states provide a bonding contribution to the pair of atoms, while a more positive COHP coefficient indicates that the Kohn–Sham state provides a more anti-bonding contribution. Fig. S21a† displays the canonical molecular orbitals of CO and their occupancies. These molecular orbitals are commonly divided among σ- and π-type orbitals based on the presence or absence of a nodal plane alongside the C–O bonding axis. It can be readily observed that the number of valence electrons of CO in the gas phase corresponds to 10. From Fig. S21f,† the bonding character for each of the orbitals is seen including the integrated COHP (iCOHP) at the Fermi level which is a quantitative measure of the C–O bond strength. Upon adsorption, we can see from Fig. S24a and c† that the 3σ and 4σ interactions are largely unchanged due to a limited mixing of these molecular orbitals with the d-orbitals on Ni. In contrast, the 1π and 5σ orbitals show pronounced mixing as evidenced by the broadening of the peaks. Furthermore, due to the mixing of the anti-bonding 2π* orbitals with the d-orbitals on Ni, the newly formed states derived from these orbitals descent below the Fermi level and become occupied. The integrated DOS (iDOS) at the Fermi level for adsorbed CO shows that the electron density around CO increases, in line with the higher electronegativity

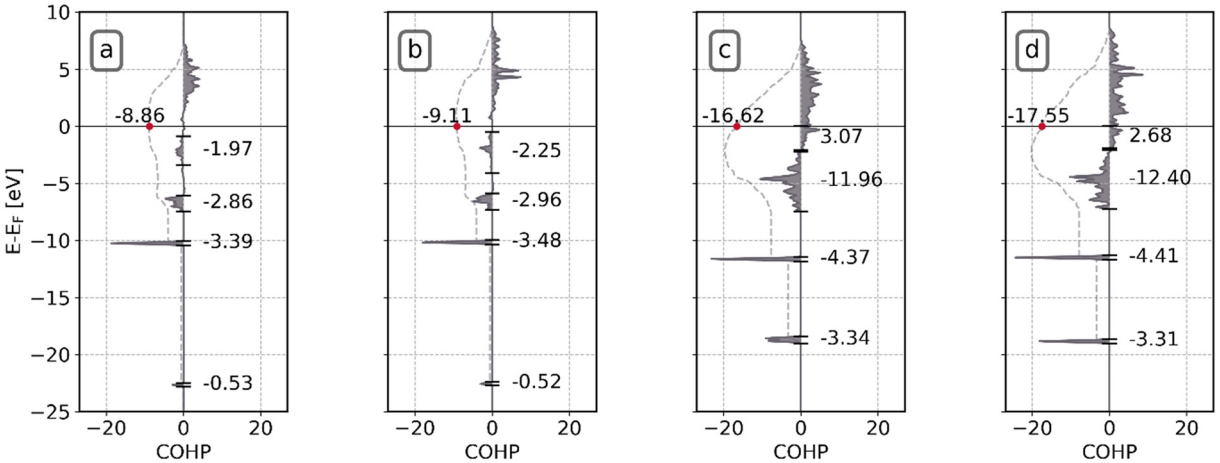

Fig. 10 COHP analysis of Ni–CO bonds in the initial state (IS) and transition state (TS) of CO direct dissociation on Ni_8/TiO_2-a and Ni_8/TiO_2-r. (a) IS on Ni_8/TiO_2-a; (b): IS on Ni_8/TiO_2-r; (c) TS on Ni_8/TiO_2-a; (d): TS on Ni_8/TiO_2-r. The numeric values above Fermi level indicate the integrated COHP (iCOHP).

of CO as compared to Ni and resulting in the occupation of the anti-bonding orbitals. The occupation of these anti-bonding orbitals together with the reduction in bonding character of the 1π-type orbitals lead to an activation of the CO molecule, as evidenced by the reduced iCOHP value shown in Fig. S21† corresponding to −15.86 and −16.09 for Ni_8/TiO_2-a and Ni_8/TiO_2-r, respectively. These values are however sufficiently similar that we cannot attribute the difference in the dissociation barrier to a difference in the activation of the CO molecule upon adsorption. The C–O interaction in the transition state, as shown in Fig. S21,† are also substantially similar from which we infer that both clusters have the same propensity towards activating CO and we hypothesize that the difference in the CO dissociation barrier should therefore be caused by differences in the stabilization of the pre-dissociated fragments in the transition state. It should be noted that this result contrasts with CO activation patterns typically found for extended metals, as showcased in the work of Fariduddin *et al.*[73]

To test our hypothesis, in Fig. 10a–d, a COHP analysis is conducted for the Ni–CO interaction. Similar to the results found for the C–O interaction, here the COHP acts as a metric to assess the interaction strength between the cluster and the C* and O* fragments. The iCOHP values for adsorbed CO*, *i.e.* in the initial state, at the Fermi level are −8.86 and −9.11 for Ni_8/TiO_2-a and Ni_8/TiO_2-r. These values are in line with the observed adsorption heats of −2.14 eV and −2.54 eV for Ni_8/TiO_2-a and Ni_8/TiO_2-r, respectively. For the transition state, significantly lower iCOHP values of −16.62 and −17.55 are found for Ni_8/TiO_2-a and Ni_8/TiO_2-r, respectively. Clearly, Ni_8/TiO_2-r shows a significant increase in the Ni–CO interaction strength between the TS and IS in comparison to Ni_8/TiO_2-a, explaining the much lower reaction barrier observed. We attribute this enhanced bonding interaction of pre-dissociated C* and O* in the transition state on Ni_8/TiO_2-r to the presence of a very stable fivefold adsorption site for C, whereas for Ni_8/TiO_2-a a less favorable quasi-fourfold adsorption site is present (as shown in Fig. S25†). This five-fold site of Ni_8/TiO_2-r hosts a square-planar motif for which exceptional stability for C* has been identified earlier in the work of Nandula *et al.*[74]

Conclusively, a critical factor in the preferred kinetic pathway is assigned to the presence of a low CO dissociation barrier. In the absence of such a barrier, a H-assisted route is preferred as seen for Ni_8/TiO_2-a. In contrast, Ni_8/TiO_2-r allows for a direct CO dissociation due to the availability of an active motif for which the COHP analysis predicts enhanced stability for the dissociation fragments.

4. Conclusions

In this study, the effect of the TiO_2 phase, anatase or rutile, on CO_2 hydrogenation over small Ni_8 cluster was investigated. Using a hybrid genetic algorithm/density functional theory approach, the putative global minimum structure for Ni_8 clusters supported on the most stable anatase and rutile surface terminations were searched. Due to different metal–support interactions, the Ni_8 clusters adopt different morphologies on anatase and rutile TiO_2.

By means of density functional theory calculations, all elementary reaction steps relevant to CO_2 hydrogenation, *i.e.* direct and H-assisted CO_2 and CO dissociation as well as subsequent hydrogenation steps to form CH_4 and CH_3OH were calculated. By means of microkinetic modelling, we observed that the anatase supported Ni_8 clusters yielded a higher activity towards CO_2 consumption as compared to the rutile equivalent. For both clusters, at the low temperature the selectivity is mainly towards CH_4 whereas with increasing temperature, the selectivity switches to CO. The amount of CH_3OH produced remains negligible.

Both catalysts exhibit direct CO_2 dissociation. Ni_8/TiO_2-r shows direct dissociation whereas for Ni_8/TiO_2-a the H-assisted route *via* a HCO* intermediate is preferred. Analysis of the reaction energy diagram and the DFT calculations reveal that this difference can be assigned to the stronger adsorption for carbonaceous species on Ni_8/TiO_2-r as compared to Ni_8-TiO_2-a. Not only leads this to a lower barrier for direct dissociation for the former catalyst, it also leads to the reaction intermediates being too strongly bound to the catalyst, effectively deactivating the catalyst. This rationalizes the consistent lower activity observed for Ni_8-TiO_2-r.

Analysis of the kinetic network pinpoints the CO dissociation barrier playing a critical role in determining the overall activity and mechanistic route. To understand the underlying electronic effects leading to the difference in CO dissociation barrier between the anatase and rutile supported Ni_8 clusters, a combined density of states and crystal orbital Hamilton population analysis was conducted. The integrated COHP value for the Ni–CO interaction at the Fermi level for the transition states for these two structures reveal that CO is more tightly bound to Ni_8 supported on rutile as compared to a cluster supported on anatase. This is not caused by electronic metal support interactions but rather by the different morphology of the cluster. For Ni_8/TiO_2-r, the morphology allows for highly stable fivefold-coordinated CO whereas for Ni_8/TiO_2-a, only a fourfold-coordinated mode is available which leads to less strongly bound CO.

This study showcases the potential role the support has in affecting the preferred pathway, selectivity and activity of a catalyst by inducing a preferred morphology of adsorbed clusters.

Data availability

The data supporting this article have been included as part of the ESI.†

Author contributions

Lulu Chen: conceptualization, data curation, formal analysis, investigation, validation, visualization, writing-original draft; Ying-Ying Ye: data curation, formal analysis, investigation,

visualization; Rozemarijn D. E. Krösschell: data curation, formal analysis visualization; Emiel J. M. Hensen: conceptualization, supervision, writing-review & editing, funding acquisition; Ivo A. W. Filot: conceptualization, methodology, resource, visualization, supervision, writing-review & editing, funding acquisition.

Conflicts of interest

The authors declare that there are no conflicts of interest regarding the publication of this paper.

Acknowledgements

We gratefully acknowledge the financial support provided by the China Scholarship Council. We also thank NWO and SurfSARA for granting the computational resources used to perform the DFT calculations.

References

1 C. Vogt, M. Monai, G. J. Kramer and B. M. Weckhuysen, *Nat. Catal.*, 2019, 2.
2 J. C. Navarro, M. A. Centeno, O. H. Laguna and J. A. Odriozola, *Catalysts*, 2018, 8.
3 L. Guerra, S. Rossi, J. Rodrigues, J. Gomes, J. Puna and M. T. Santos, *J. Environ. Chem. Eng.*, 2018, **6**, 671–676.
4 K. Müller, M. Städter, F. Rachow, D. Hoffmannbeck and D. Schmeißer, *Environ. Earth Sci.*, 2013, **70**, 3771–3778.
5 S. Chen and A. M. Abdel-Mageed, *Int. J. Hydrogen Energy*, 2013, **48**, 24915–24935.
6 M. Götz, J. Lefebvre, F. Mörs, A. McDaniel Koch, F. Graf, S. Bajohr, R. Reimert and T. Kolb, *Renewable Energy*, 2016, **85**, 1371–1390.
7 M. Lehner, R. Tichler, H. Steinmüller and M. Koppe, *Power-to-Gas: Technology and Business Models*, Springer Briefs in Energy, 2014.
8 F. Graf, *Impact*, 2018, **2018**, 81–83.
9 O. Mohan, S. Shambhawi, R. Xu, A. A. Lapkin and S. H. Mushrif, *ChemCatChem*, 2021, **13**, 2420–2433.
10 P. Frontera, A. Macario, M. Ferraro and P. L. Antonucci, *Catalysts*, 2017, **7**, 59.
11 A. Quindimil, U. De-La-Torre, B. Pereda-Ayo, A. Davó-Quiñonero, E. Bailón-García, D. Lozano-Castelló, J. A. González-Marcos, A. Bueno-López and J. R. González-Velasco, *Catal. Today*, 2020, **356**, 419–432.
12 A. Parastaev, V. Muravev, E. H. Osta, T. F. Kimpel, J. F. M. Simons, A. J. F. van Hoof, E. Uslamin, L. Zhang, J. J. C. Struijs, D. B. Burueva, E. V. Pokochueva, K. V. Kovtunov, I. V. Koptyug, I. J. Villar-Garcia, C. Escudero, T. Altantzis, P. Liu, A. Béché, S. Bals, N. Kosinov and E. J. M. Hensen, *Nat. Catal.*, 2022, **5**, 1051–1060.
13 Z. Liu, X. Gao, B. Liu, W. Song, Q. Ma, T. s. Zhao, X. Wang, J. W. Bae, X. Zhang and J. Zhang, *Appl. Catal., B*, 2022, **310**, 121303.
14 S. Tada, T. Shimizu, H. Kameyama, T. Haneda and R. Kikuchi, *Int. J. Hydrogen Energy*, 2012, **37**, 5527–5531.
15 R. van Hardeveld and A. van Montfoort, *Surf. Sci.*, 1966, **4**, 396–430.
16 G. Melaet, A. E. Lindeman and G. A. Somorjai, *Top. Catal.*, 2014, **57**, 500–507.
17 X. Wang, H. Shi, J. H. Kwak and J. Szanyi, *ACS Catal.*, 2015, **5**, 6337–6349.
18 V. Iablokov, S. K. Beaumont, S. Alayoglu, V. V. Pushkarev, C. Specht, J. Gao, A. Paul Alivisatos, N. Kruse and G. A. Somorjai, *Nano Lett.*, 2012, **12**, 3091–3096.
19 J. H. Kwak, L. Kovarik and J. Szanyi, *ACS Catal.*, 2013, **3**, 2449–2455.
20 P. Panagiotopoulou, *Appl. Catal., A*, 2017, **542**, 63–70.
21 N. L. Visser, O. Daoura, P. N. Plessow, L. C. J. Smulders, J. W. de Rijk, J. A. Stewart, B. D. Vandegehuchte, F. Studt, J. E. S. van der Hoeven and P. E. de Jongh, *ChemCatChem*, 2022, **14**, e202200665.
22 C. Vogt, E. Groeneveld, G. Kamsma, M. Nachtegaal, L. Lu, C. J. Kiely, P. H. Berben, F. Meirer and B. M. Weckhuysen, *Nat. Catal.*, 2018, **1**, 127–134.
23 C. Vogt, F. Meirer, M. Monai, E. Groeneveld, D. Ferri, R. A. van Santen, M. Nachtegaal, R. R. Unocic, A. I. Frenkel and B. M. Weckhuysen, *Nat. Commun.*, 2021, **12**, 7096.
24 Y. Guo, S. Mei, K. Yuan, D. J. Wang, H. C. Liu, C. H. Yan and Y. W. Zhang, *ACS Catal.*, 2018, **8**, 6203–6215.
25 E. J. M. H. Jérôme, F. M. Simons, T. J. de Heer, R. C. J. van de Poll, V. Muravev and N. Kosinov, *J. Am. Chem. Soc.*, 2023, **145**, 20289–20301.
26 M. P. C. Van Etten, B. Zijlstra, E. J. M. Hensen and I. A. W. Filot, *ACS Catal.*, 2021, **11**, 8484–8492.
27 S. Liang, C. Hao and Y. Shi, *ChemCatChem*, 2015, **7**, 2559–2567.
28 R. Zhou, N. Rui, Z. Fan and C. Liu, *Int. J. Hydrogen Energy*, 2016, **41**, 22017–22025.
29 C.-J. Pan, M.-C. Tsai, W.-N. Su, J. Rick, N. G. Akalework, A. K. Agegnehu, S.-Y. Cheng and B.-J. Hwang, *J. Taiwan Inst. Chem. Eng.*, 2017, **74**, 154–186.
30 W. Li, G. Zhang, X. Jiang, Y. Liu, J. Zhu, F. Ding, Z. Liu, X. Guo and C. Song, *ACS Catal.*, 2019, **9**, 2739–2751.
31 Y. Lin, Y. Zhu, X. Pan and X. Bao, *Catal. Sci. Technol.*, 2017, **7**, 2813–2818.
32 J. Zhou, Z. Gao, G. Xiang, T. Zhai, Z. Liu, W. Zhao, X. Liang and L. Wang, *Nat. Commun.*, 2022, **13**, 327.
33 D. Messou, V. Bernardin, F. Meunier, M. B. Ordoño, A. Urakawa, B. F. Machado, V. Collière, R. Philippe, P. Serp and C. Le Berre, *J. Catal.*, 2021, **398**, 14–28.
34 M. P. C. Van Etten, M. E. De Laat, E. J. M. Hensen and I. A. W. Filot, *J. Phys. Chem. C*, 2023, **127**, 15148–15156.
35 J. P. Perdew, K. Burke and M. Ernzerhof, *Phys. Rev. Lett.*, 1996, **77**, 3865–3868.
36 G. Kresse and J. Furthmüller, *Comput. Mater. Sci.*, 1996, **6**, 15–50.
37 G. Kresse and J. Furthmüller, *Phys. Rev. B: Condens. Matter Mater. Phys.*, 1996, **54**, 11169.
38 P. E. Blöchl, *Phys. Rev. B: Condens. Matter Mater. Phys.*, 1994, **50**, 17953–17979.
39 D. Joubert, *Phys. Rev. B: Condens. Matter Mater. Phys.*, 1999, **59**, 1758–1775.
40 P. W. Fry, I. E. Itskevich, S. R. Parnell, J. J. Finley, L. R. Wilson, K. L. Schumacher, D. J. Mowbray, M. S. Skolnick,

A. G. Cullis, M. Hopkinson, J. C. Clark and G. Hill, *Phys. Rev. B: Condens. Matter Mater. Phys.*, 2000, **62**, 784–791.
41 S. Grimme, J. Antony, S. Ehrlich and H. Krieg, *J. Chem. Phys.*, 2010, **132**, 154104.
42 S. Grimme, S. Ehrlich and L. Goerigk, *J. Comput. Chem.*, 2011, **32**, 1456–1465.
43 G. Henkelman, B. P. Uberuaga and H. Jónsson, *J. Chem. Phys.*, 2000, **113**, 9901–9904.
44 G. Henkelman and H. Jónsson, *J. Chem. Phys.*, 2000, **113**, 9978–9985.
45 N. Martsinovich and A. Troisi, *Phys. Chem. Chem. Phys.*, 2012, **14**, 13392–13401.
46 D. H. M. Azevedo, G. S. L. Fabris, J. R. Sambrano and J. M. M. Cordeiro, *Comput. Mater. Sci.*, 2020, **171**, 109222.
47 R. D. E. Krösschell, E. J. M. Hensen and I. A. W. Filot, *J. Phys. Chem. C*, 2024, **128**, 8947–8960.
48 C. J. Howard, T. M. Sabine and F. Dickson, *Acta Crystallogr., Sect. B: Struct. Sci.*, 1991, **47**, 462–468.
49 S. Wu, X. Luo, Y. Long and B. Xu, *IOP Conf. Ser.: Mater. Sci. Eng.*, 2019, **493**, 012010.
50 S. Ma, W. Song, B. Liu, H. Zheng, J. Deng, W. Zhong, J. Liu, X. Q. Gong and Z. Zhao, *Catal. Sci. Technol.*, 2016, **6**, 6128–6136.
51 L. B. Vilhelmsen and B. Hammer, *J. Chem. Phys.*, 2014, **141**, 044711.
52 M. W. Chang, L. Zhang, M. Davids, I. A. W. Filot and E. J. M. Hensen, *J. Catal.*, 2020, **392**, 39–47.
53 L. Van Der Maaten and G. Hinton, *J. Mach. Learn. Res.*, 2008, **9**, 2579–2605.
54 F. Pedregosa, G. Varoquaux, A. Gramfort, V. Michel, B. Thirion, O. Grisel, M. Blondel, A. Müller, J. Nothman, G. Louppe, P. Prettenhofer, R. Weiss, V. Dubourg, J. Vanderplas, D. Cournapeau, M. Brucher and M. Perrot, *J. Mach. Learn. Res.*, 2011, **12**, 2825–2830.
55 I. Gohberg, S. Goldberg and M. A. Kaashoek, *Classes of Linear Operators*, Birkhäuser Basel, Basel, 1990, vol. I, pp. 138–147.
56 I. A. W. Filot, M. P. C. van Etten, D. W. J. G. Trommelen and E. J. M. Hensen, *J. Open Source Softw.*, 2023, **8**, 5710.
57 I. A. W. Filot, *Introduction to microkinetic modeling*, Technische Universiteit Eindhoven, 2018.
58 I. A. W. Filot, R. A. Van Santen and E. J. M. Hensen, *Angew. Chem., Int. Ed.*, 2014, **53**, 12746–12750.
59 P. Nitoń, A. Zywociński, M. Fiałkowski and R. Hołyst, *Nanoscale*, 2013, **5**, 9732–9738.
60 W. L. Vrijburg, E. Moioli, W. Chen, M. Zhang, B. J. P. Terlingen, B. Zijlstra, I. A. W. Filot, A. Züttel, E. A. Pidko and E. J. M. Hensen, *ACS Catal.*, 2019, **9**, 7823–7839.
61 C. T. Campbell, *Top. Catal.*, 1994, **1**, 353–366.
62 F. Cannizzaro, E. J. M. Hensen and I. A. W. Filot, *ACS Catal.*, 2023, **13**, 1875–1892.
63 Q. Ke, L. Kang, X. Chen and Y. Wu, *Chem. Sci. J.*, 2020, **132**, 1–11.
64 A. Mahdavi-Shakib, T. N. Whittaker, T. Y. Yun, K. B. Sravan Kumar, L. C. Rich, S. Wang, R. M. Rioux, L. C. Grabow and B. D. Chandler, *Nat. Catal.*, 2023, **6**, 710–719.
65 E. B. Sterk, A. E. Nieuwelink, M. Monai, J. N. Louwen, E. T. C. Vogt, I. A. W. Filot and B. M. Weckhuysen, *JACS Au*, 2022, **2**, 2714–2730.
66 J. Zhang, Y. Yang, J. Liu and B. Xiong, *Appl. Surf. Sci.*, 2021, **558**, 149866.
67 J. Liu, C. Li, F. Wang, S. He, H. Chen, Y. Zhao, M. Wei, D. G. Evans and X. Duan, *Catal. Sci. Technol.*, 2013, **3**, 2627–2633.
68 M. A. Abir, R. E. Phillips, J. Z. M. Harrah and M. R. Ball, *Catal. Sci. Technol.*, 2024, **14**, 4506–4521.
69 J.-Y. Li, X.-M. Lai, H. Gu, C.-X. Wang, X.-P. Fu, W.-W. Wang, Q. Fu, F. Ryan Wang, C. Ma and C.-J. Jia, *ChemRxiv*, 2023, preprint, DOI: **10.26434/chemrxiv-2023-bm0gl**.
70 F. Abild-Pedersen and M. P. Andersson, *Surf. Sci.*, 2007, **601**, 1747–1753.
71 J. Wellendorff, T. L. Silbaugh, D. Garcia-Pintos, J. K. Nørskov, T. Bligaard, F. Studt and C. T. Campbell, *Surf. Sci.*, 2015, **640**, 36–44.
72 O. Mohan, Q. T. Trinh, A. Banerjee and S. H. Mushrif, *Mol. Simul.*, 2019, **45**, 1163–1172.
73 I. A. W. Filot, F. Fariduddin, R. J. P. Broos, B. Zijlstra and E. J. M. Hensen, *Catal. Today*, 2016, **275**, 111–118.
74 A. Nandula, Q. T. Trinh, M. Saeys and A. N. Alexandrova, *Angew. Chem., Int. Ed.*, 2015, **54**, 5312–5316.